

An Analytical Model for Analyzing and Forecasting Production From Multifractured Horizontal Wells With Complex Branched-Fracture Geometry

M. Heidari Sureshjani, IOR Research Institute, and C. R. Clarkson, University of Calgary

Summary

Analytical methods for analyzing and forecasting production from multifractured horizontal wells completed in unconventional reservoirs are in their infancy. Among the difficulties in modeling such systems is the incorporation of fracture-network complexity as a result of the hydraulic-fracturing process. Along with a primary propped-hydraulic-fracture network, a secondary fracture network, which may or may not contain proppant, may be activated during the stimulation process, creating a “branched-fracture” network. These secondary fractures can be the result of reactivation of healed natural fractures, for example.

In the current work, we develop a fully analytical enhanced-fracture-region (EFR) model for analyzing and forecasting multifractured horizontal wells with complex fracture geometry that is more-general, -rigorous, and -flexible than those previously developed. Specifically, our new model allows nonsymmetric placement of a well within its area of drainage, to reflect unequal horizontal-lateral spacing; this is a very real scenario observed in the field, particularly for the external laterals on a pad. The solutions also can be reduced to be applicable for homogeneous systems without branch fractures. In addition to the general EFR solution, we have provided local solutions that can be used to analyze individual flow regimes in sequence. We provide practical examples of the application (and sometimes misapplication) of local solutions by use of simulated and field cases. One important observation is that a negative intercept obtained from a straight line drawn through data on a square-root-of-time plot (commonly used to analyze transient linear flow) may indicate EFR behavior, but this straight line should not be interpreted as linear flow because it represents transitional flow from one linear-flow period to another.

Our general EFR solution therefore provides a powerful tool to improve both forecasting and flow-regime interpretation for hydraulic-fracture/reservoir characterization.

Introduction

Multifractured horizontal wells (MFHWs), although they enable commercial production from low-permeability reservoirs, are a challenge to analyze and forecast for petroleum engineers. To capture many of the complexities of the well, fracture and reservoir geometries and properties, the analyst has had to resort to numerical simulation, which is time-consuming to apply and is often not supported by available data sets. Analytical forecasting tools are simpler to set up, but often are not flexible enough to capture a complete range of reservoir/fracture behaviors.

Two analytical models that have emerged in the past several years that are quite commonly used include the trilinear-flow (TLF) model (Brown et al. 2011; Ozkan et al. 2011) and the enhanced-fracture-region (EFR) model (Stalgorova and Mattar 2013). These models represent an excellent attempt to capture a greater range of reservoir and fracture properties associated with

MFHWs completed in low-permeability formations. The TLF and EFR models have been successfully applied to model complex well behavior exhibited in the field (Stalgorova and Mattar 2012; Samandarli et al. 2014). Very importantly, these models have also been used in parallel with local (straight-line) solutions for reservoir and hydraulic-fracture characterization. Local (straight-line) solutions are simply solutions to the flow equations for a specific flow regime, such as linear flow (LF), radial flow, and boundary-dominated flow. However, because multiple flow regimes can be observed, and it is possible for more than one LF period to appear during production, local solutions can be misapplied, resulting in incorrect information being extracted. Because the more-general solutions (such as the TLF and EFR models) can model the full suite of flow regimes in sequence, they can also be used to prevent misapplication of the local solutions.

Although the TLF and EFR models have significantly advanced analytical modeling for unconventional reservoirs, they are still not flexible enough to capture some behaviors of importance to analysts. For example, MFHWs are often drilled in sets off of a pad, with laterals drilled parallel to each other. These laterals may not be equally spaced, as assumed in existing analytical models, meaning that their area of drainage is not symmetrical. Furthermore, the TLF solution is only applicable where the stimulated region completely covers the interfracture region. Although the EFR model introduced by Stalgorova and Mattar (2013) has solved this problem by being able to model cases where branch fractures partially cover the interfracture region, it is not valid for all ranges of parameters, as mentioned in their study. It may not also represent the signature of different flow regimes for some cases.

In this work, we introduce an EFR model that is more general and rigorous than previous models. This new model is capable of capturing a broader range of reservoir/fracture properties and flow-regime sequences than before. We also provide local (straight-line) solutions that are applicable to each flow regime. A sensitivity study is performed to illustrate various controls on flow-regime sequences and behaviors. Finally, we demonstrate practical application of our new model to prevent misinterpretation of flow regimes, and misapplication of local solutions, by use of simulated and field cases.

Mathematical Model

Fig. 1 illustrates the physical model used as the basis for the mathematical model developed in this work. The dimensions of the physical model are shown in Fig. 2. As Fig. 2 illustrates, the fracture length on both sides of the well is equal to x_f . However, the well is not necessarily centered in the reservoir in the x -direction. The distance of the well from one boundary is x_1 and from the opposite boundary is x_2 . To derive production rates for this system, we subdivide the model into five subsystems that are linked to each other through boundary conditions (Fig. 3). The stimulated region is labeled “S” and fracture region is labeled “F.” The unstimulated area is divided into three regions (Regions 1, 2, and 3), as can be seen in Fig. 3. Fig. 3 also shows the coordinates of each region. Here, we present the analytical solution for

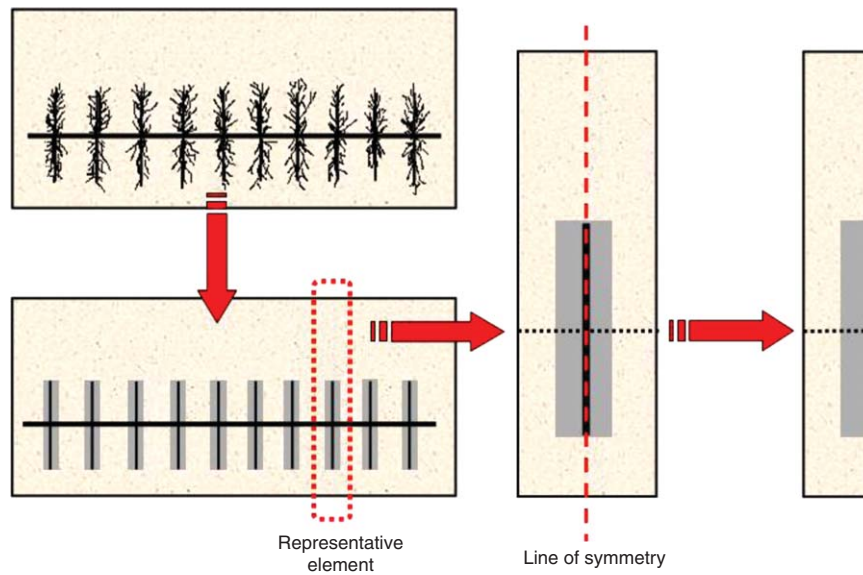


Fig. 1—Idealization and simplification of physical model.

infinite-conductivity- and finite-conductivity-fracture cases corresponding to this physical model.

For the infinite-fracture-conductivity case, the fracture is regarded as the constant-pressure boundary condition. In this case, we solve the governing differential equation of the stimulated region. The governing equation and boundary conditions for the stimulated region in Laplace space are written as

$$\frac{\partial^2 \bar{p}_{Ds}}{\partial y_D^2} - \frac{R_k}{2} \left(\frac{\partial \bar{p}_{D2}}{\partial x_D} \right)_{x_D=x_{D1}-1} - \frac{R_k}{2} \left(\frac{\partial \bar{p}_{D3}}{\partial \theta_D} \right)_{\theta_D=x_{D2}-1} - s R_{\eta} \bar{p}_{Ds} = 0, \quad \dots \dots \dots (1)$$

$$\bar{p}_{Ds} = \frac{1}{s}, \quad y_D = 0, \quad \dots \dots \dots (2)$$

$$\bar{p}_{Ds} = \bar{p}_{D1}(y_{D1}) = \bar{p}_{D1s}, \quad y_D = y_{Ds}. \quad \dots \dots \dots (3)$$

Definitions for dimensionless parameters are given in **Table 1**. In Eq. 1, the first term is representative of mass flow in the y -direction toward the fracture in the stimulated region. The second term represents the mass flux exiting Region 2 and entering the stimulated region. Likewise, the third term accounts for mass exchange between Region 3 and the stimulated region. Finally, the last term is accumulation of mass in any element of the stimulated region in the y -direction. For the situation where Regions 2 and 3 are relatively small, the second and third terms can be ignored. The first boundary condition (Eq. 2) represents a constant-pressure condition in the fracture. Because the fracture is assumed to have infinite conductivity, the fracture pressure is considered to be equal to wellbore pressure. The second boundary condition simply states that the pressure at distance y_1 is the pressure at the interface of the stimulated region and Region 1. Mass exchange between Region 2 (or Region 3) and the stimulated region has been considered in the partial differential equation (Eq. 1), whereas fluid transfer across the interface of the stimulated

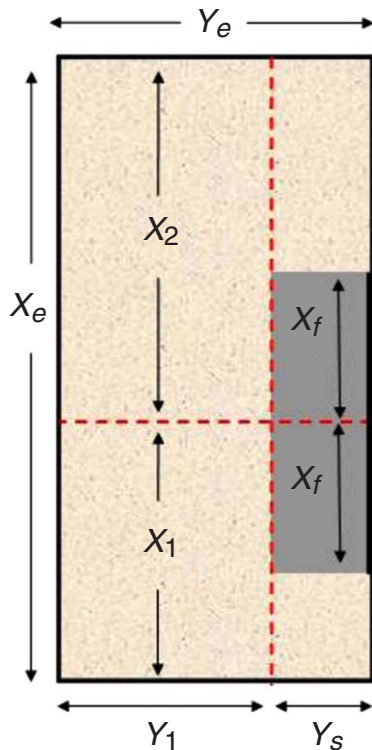


Fig. 2—Dimensions of physical model.

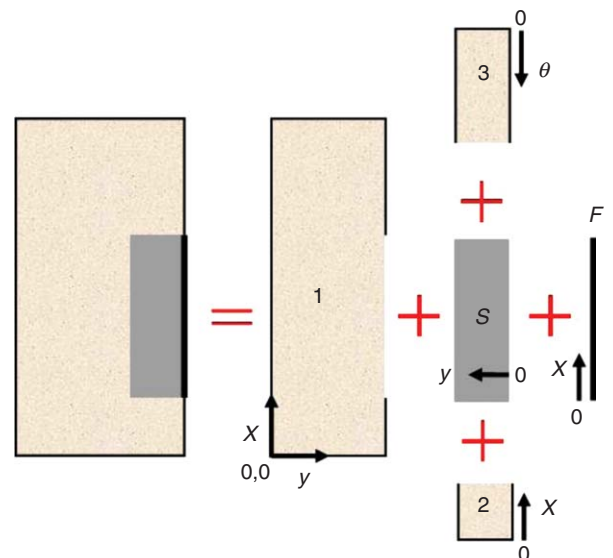


Fig. 3—Breaking the physical model into five parts: The pressure solution in each part is linked to adjacent parts through boundary conditions.

$$\begin{aligned}
p_D &= \frac{p_i - p}{p_i - p_w} & q_D &= \frac{\mu B}{2kh(p_i - p)} q \\
t_D &= \frac{kt}{\mu c_f \phi x_f^2} & p_{D1s,u} &= \frac{2kh}{q\mu B} \Delta p_{1s,u} \\
x_D &= \frac{x}{x_f} & y_D &= \frac{y}{x_f} \\
\theta_D &= \frac{\theta}{x_f} & R_\eta &= \frac{\eta}{\eta_s} \\
R_k &= \frac{k}{k_s} & F_{CDs} &= \frac{wk_f}{k_s x_f} \\
F_{CD} &= \frac{wk_f}{x_f k} & R_{\eta f} &= \frac{\eta}{\eta_f}
\end{aligned}$$

Table 1—Definition of dimensionless parameters.

region and Region 1 was taken into account through the boundary condition (Eq. 3). It must be emphasized that in Regions 2 and 3 we considered one-dimensional flow toward the stimulated region. Accordingly, we only require two boundary conditions for each region; that is, we assumed the boundary between Region 2 (or Region 3) and Region 1 is acting like a no-flow boundary. This assumption will be very helpful in deriving the solutions.

To solve Eq. 1, we must first determine solutions for Regions 2 and 3 and include their derivative in Eq. 1. The solution for produced rate into the fracture for the infinite-conductivity-fracture case is then obtained as

$$\bar{q}_{Dw} = \frac{2\sqrt{a_1}(a_3 - \bar{p}_{D1s})}{R_k s a_2} \quad (4)$$

Parameters a_1 through a_3 can be found in **Table 2**. The derivation of Eq. 4 is presented in Appendix A.

For the finite-conductivity-fracture case, we solve the governing equation in the fracture region. The differential equation, along with boundary conditions for the fracture, is given as

$$\frac{\partial^2 \bar{p}_{Df}}{\partial x_D^2} + \frac{2}{F_{CDs}} \left(\frac{\partial \bar{p}_{Ds}}{\partial y_D} \right)_{y_D=0} - s R_{\eta f} \bar{p}_{Df} = 0, \quad (5)$$

$$\frac{\partial \bar{p}_{Df}}{\partial x_D} = 0, \quad x_D = 0, \quad (6)$$

$$\bar{p}_{Df} = \frac{1}{s}, \quad x_D = 1. \quad (7)$$

The first, second, and third terms in Eq. 5 represent mass flow in the fracture toward the well, mass flow feeding from the stimulated region into the fracture, and mass accumulation in any element of the fracture, respectively. Because the fracture has a very small width and high permeability compared with the region near the tips of fracture, the mass rate from Regions 2 and 3 into the tip of fracture is relatively small and can be ignored. Accordingly, the boundary condition at the tips of fracture is assumed to be a no-flow boundary, as represented by Eq. 6. Because the well is producing at constant bottomhole pressure, one can consider Eq. 7 as the inner-boundary condition of fracture region. The solution for production rate is then derived as

$$\bar{q}_{Dw} = F_{CD} a_7 (a_5 - s a_6 \bar{p}_{D1s}). \quad (8)$$

Parameters a_5 through a_7 are given in Table 2. Details of the derivation of Eq. 8 are given in Appendix B. It should be noted that Eq. 8 applies to the situation where flow is completely linear in the fracture. In actual situations, flow in the fracture in the vicinity of wellbore is radial. This may cause an additional pressure

$$\begin{aligned}
a_1 &= \frac{R_k \sqrt{s}}{2} \left\{ \tanh \left[\sqrt{s} (x_{D1} - 1) \right] + \tanh \left[\sqrt{s} (x_{D2} - 1) \right] \right\} + R_\eta s \\
a_2 &= \frac{\sinh(\sqrt{a_1} y_{Ds})}{s} \\
a_3 &= \frac{\cosh(\sqrt{a_1} y_{Ds})}{s} \\
a_4 &= \coth(\sqrt{a_1} y_{Ds}) \\
a_5 &= \frac{2a_4 \sqrt{a_1}}{F_{CDs}} + s R_{\eta f} \\
a_6 &= \frac{2\sqrt{a_1}}{F_{CDs} s a_2} \\
a_7 &= \frac{\tanh(\sqrt{a_5})}{s \sqrt{a_5}}
\end{aligned}$$

Table 2—Definition of parameters a_1 through a_7 .

drop compared with pure linear flow in the fracture. We must consider the effect of flow convergence toward the well in the obtained solution. To do so, we use the convergence skin introduced by Mukherjee and Economides (1991). The solution considering flow convergence (caused by radial flow to the wellbore) is obtained as

$$\bar{q}_{Dw} = \frac{1}{\frac{1}{F_{CD} a_7 (a_5 - s a_6 \bar{p}_{D1s})} + \frac{s S_c}{2\pi}} \quad (9)$$

The methodology for inclusion of convergence skin into the solution is given in Appendix B.

As can be seen in Eqs. 8 and 9, we require an estimate of the pressure drop at the interface between the stimulated region and Region 1 (\bar{p}_{D1s}). To obtain an expression for pressure drop at this interface, we first determine pressure drop for withdrawal of a continuous constant unit rate from this interface. We then determine the actual pressure drop with the aid of convolution theory. To determine pressure drop per unit rate at the inner boundary of Region 1, the corresponding governing differential equation should be solved. The differential equations, with appropriate boundary conditions for Region 1, in Laplace space are

$$\frac{\partial^2 \bar{p}_{D1}}{\partial x_D^2} + \frac{\partial^2 \bar{p}_{D1}}{\partial y_D^2} - s \bar{p}_{D1} = 0, \quad (10)$$

$$\frac{\partial \bar{p}_{D1}}{\partial x_D} = 0, \quad x_D = 0, \quad 0 < y_D < y_{D1}, \quad (11)$$

$$\frac{\partial \bar{p}_{D1}}{\partial x_D} = 0, \quad x_D = x_{De}, \quad 0 < y_D < y_{D1}, \quad (12)$$

$$\frac{\partial \bar{p}_{D1}}{\partial y_D} = 0, \quad 0 < x_D < x_{De}, \quad y_D = 0, \quad (13)$$

$$\frac{\partial \bar{p}_{D1}}{\partial y_D} = \begin{cases} 0, & 0 < x_D < x_{D1} - 1, x_{D1} + 1 < x_D < x_{De} \\ \frac{1}{s}, & x_{D1} - 1 < x_D < x_{D1} + 1 \end{cases}, \quad y_D = y_{D1}. \quad (14)$$

We applied the Fourier transform to remove differentiation with respect to the x -coordinate so that the differential equation can be solved. The Fourier transform was used by Odeh (1968) for obtaining the pressure solution in wells with restricted entry to flow, but here we apply this transformation for our specific problem. The solution for pressure drop per unit rate at the inner boundary of Region 1 is obtained as

$$\bar{p}_{D1,u}(y_{D1}) = \bar{p}_{D1s,u} = \frac{2\coth(\sqrt{s}y_{D1})}{x_{De}s\sqrt{s}} + \frac{2x_{De}}{\pi^2 s} \sum_{n=1}^{\infty} \frac{\left\{ \sin\left[\frac{n\pi}{x_{De}}(x_{D1}+1)\right] - \sin\left[\frac{n\pi}{x_{De}}(x_{D1}-1)\right] \right\}^2}{n^2 \xi_n} \times \coth(\xi_n y_{D1}). \quad (15)$$

A detailed derivation of Eq. 15 is presented in Appendix C. To obtain pressure drop at the interface, we use the convolution integral:

$$\Delta p_{1s} = \int_0^t q_1(\tau) \frac{\partial \Delta p_{1s,u}(t-\tau)}{\partial \tau} d\tau, \quad (16)$$

where q_1 is flow rate exiting Region 1 and entering the stimulated region. By use of Eq. 16, the pressure drop at the interface of Region 1 and the stimulated region, for the infinite-conductivity-fracture case, is obtained as

$$\bar{p}_{D1s} = \frac{a_3 a_4 - a_2}{\frac{R_k}{s\sqrt{a_1 \bar{p}_{D1s,u}}} + a_4}. \quad (17)$$

For the finite-conductivity-fracture case, it is obtained as

$$\bar{p}_{D1s} = \frac{s a_7 (a_3 a_4 - a_2)}{\frac{R_k}{s\sqrt{a_1 \bar{p}_{D1s,u}}} + a_4 + \frac{a_6 a_2}{a_5} s - \frac{a_6 a_2 a_7}{a_5} s^2 - \frac{a_6 a_3 a_4}{a_5} s + \frac{a_6 a_7 a_3 a_4}{a_5} s^2}. \quad (18)$$

The derivations of Eqs. 17 and 18 are presented in Appendix D.

Note that for the case where there is no stimulated region, we can obtain the constant-pressure solution from the constant-rate solution (Eq. 15) with the use of the relationship reported by van Everdingen and Hurst (1949):

$$\bar{q}_{Dcp} = \frac{1}{s^2 \bar{p}_{Dcr}}. \quad (19)$$

We replace y_{D1} with y_{De} in Eq. 15 and insert it in Eq. 19 to obtain the constant-pressure solution for an infinite-conductivity fracture in a closed rectangular reservoir. It should be noticed that the obtained equation must be multiplied by two to account for production from both sides of the fracture. It is written as

$$\bar{q}_{Dw} = \frac{1}{\frac{\sqrt{s}\coth(\sqrt{s}y_{De})}{x_{De}} + \frac{s x_{De}}{\pi^2} \sum_{n=1}^{\infty} \frac{\left\{ \sin\left[\frac{n\pi}{x_{De}}(x_{D1}+1)\right] - \sin\left[\frac{n\pi}{x_{De}}(x_{D1}-1)\right] \right\}^2}{n^2 \xi_n} - \coth(\xi_n y_{De})}. \quad (20)$$

Eq. 20 could be used for determining production from a constant-pressure well intersected by an infinite-conductivity fracture with no secondary fissures.

The previous models, as well as the current model, are modeled after several simplifying assumptions. These assumptions for the present model are

- The flow in Regions 2 and 3 is considered to be 1D. This assumption is sensible because permeability of the stimulated region is higher than that of Regions 2 and 3. This promotes the formation of 1D flow in these regions.
- There is no flux across Regions 1 and 2 (as if there is a barrier between these regions) and also Regions 1 and 3.
- The flow at the interface of the stimulated region and Region 1 is assumed to be of uniform-flux type (i.e., the flux distribution across this interval is uniform and equal).

- The flow in the stimulated region is assumed to be 1D. This assumption may become less accurate when the fracture has very low conductivity.
- For the case of infinite-conductivity fractures, flux from the stimulated region across the fracture interval is uniform.
- The fracture completely penetrates the formation thickness.
- Fracture wings are equal.
- Darcy's law is applicable.

Comparing the presented model with previous ones, two assumptions have been relaxed. In previous models, the well is assumed to have equally spaced laterals, whereas in the new model the lateral spacing can be varied. Furthermore, the presented model accounts for the radial (2D) nature of flow in Region 1, whereas in the previous models this region was divided into two regions with a 1D flow assumption in each region (which are perpendicular to each other).

In shale-gas reservoirs, the stimulated region may behave as a dual-porosity system. This may happen because of the creation of new minor fractures or reactivation of healed natural fractures around the main hydraulic fracture. In this situation, the created/activated fractures in the stimulated region are regarded as the main conduit of flow and the matrix blocks are sources that feed fluids into fractures. Accordingly, this region may behave as a dual-porosity system. The governing differential equation in the stimulated zone in Laplace space becomes

$$\frac{\partial^2 \bar{p}_{Ds}}{\partial y_D^2} - \frac{R_k}{2} \left(\frac{\partial \bar{p}_{D2}}{\partial x_D} \right)_{x_D=x_{D1}-1} - \frac{R_k}{2} \left(\frac{\partial \bar{p}_{D3}}{\partial \theta_D} \right)_{\theta_D=x_{D2}-1} - s R_\eta F(s) \bar{p}_{Ds} = 0. \quad (21)$$

In Eq. 21, $R_\eta = \eta/\eta_s$, where η_s is defined as

$$\eta_s = \frac{k_{fb}}{\mu[(\phi c_t)_f + (\phi c_t)_m]}. \quad (22)$$

When using the Warren and Root (1963) pseudosteady-state approach for modeling matrix/fracture fluid transfer, function $F(s)$ is obtained as

$$F(s) = \frac{\lambda + s\omega R_\eta(1-\omega)}{\lambda + s R_\eta(1-\omega)}, \quad (23)$$

where

$$\lambda = \sigma x_f^2 \frac{k_m}{k_{fb}} \quad (24)$$

and

$$\omega = \frac{(\phi c_t)_f}{(\phi c_t)_m + (\phi c_t)_f}. \quad (25)$$

In Eq. 24, σ is the shape factor, which is a function of matrix-block geometry. The mathematical expression for parameter a_1 , which is provided in Table 2, is then changed to

$$a_1 = \frac{R_k \sqrt{s}}{2} \{ \tanh[\sqrt{s}(x_{D1}-1)] + \tanh[\sqrt{s}(x_{D2}-1)] \} + R_\eta s F(s). \quad (26)$$

The matrix/fracture fluid exchange also can be modeled by use of the de Swaan O. (1976) transient approach, which will lead to a different expression for $F(s)$. Both pseudosteady-state and transient models, as well as their application in shale-gas reservoirs, are elaborately discussed and derived in Brown et al. (2011).

Verification

To verify the solutions developed previously, we have prepared several numerical models by use of commercial software to perform comparisons with the analytical solutions. The distance perpendicular to the fracture is gridded logarithmically to ensure accurate modeling of flow toward the fracture. We used 122 grid

Initial pressure, p_i (psia)	4,000
Wellbore pressure, p_w (psia)	1,500
Oil viscosity, μ (cp)	1
Total compressibility, c_t (1/psia)	0.5×10^{-5}
Oil formation volume factor, B (bbl/STB)	1.2
Initial water saturation, S_w (fraction)	0
Thickness, h (ft)	100
Wellbore radius, r_w (ft)	0.3
Fracture half-length, x_f (ft)	125
Reservoir size in x -direction, x_e (ft)	1,050
Reservoir size in y -direction, y_e (ft)	100
Fracture opening, w (ft)	0.0013
Porosity of unstimulated region, ϕ (fraction)	0.07
Porosity of stimulated region, ϕ_s (fraction)	0.12
Porosity of fracture, ϕ_f (fraction)	0.40
Permeability of unstimulated region, k (md)	0.0005
Permeability of stimulated region, k_s (md)	0.001

Table 3—Properties used in simulation examples.

	Example 1	Example 2	Example 3
Type (composite/homogeneous)	Composite	Composite	Homogeneous
Type (infinite/finite conductivity)	Infinite	Finite	Infinite
Fracture permeability, k_f (md)	Infinite	2,000	Infinite
Distance from wellbore to one side of reservoir, x_1 (ft)	375	375	375
Stimulated distance, y_s (ft)	18	18	0

Table 4—Other properties for simulation examples.

Effective (bulk) fracture permeability (md)	0.001
Effective fracture porosity	0.01
Matrix permeability (md)	0.0002
Matrix porosity	0.07
Shape factor (ft^{-2})	0.1

Table 5—Properties for Example 4 (stimulated region is dual porosity). The other properties are similar to those of Example 1.

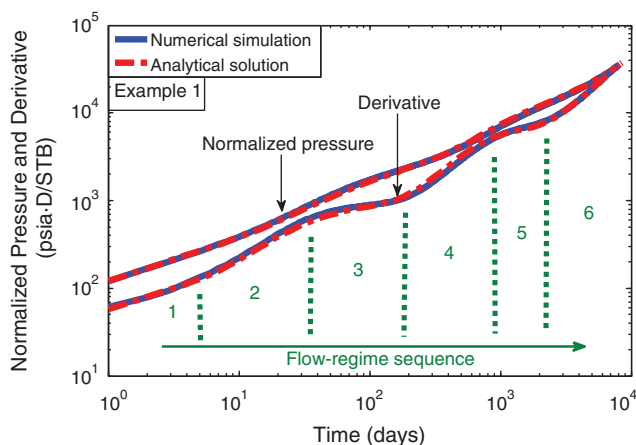


Fig. 4—Comparison of numerical simulation and analytical solution: Example 1.

cells in the y -direction (the direction perpendicular to the fracture) and 21 grid cells in the x -direction (the direction parallel to the fracture). Although the fracture penetrates the entire formation, we used 11 grid cells in the z -direction to ensure accurate modeling of flow convergence toward the well in the fracture. Our sensitivity analysis with respect to the number of grid cells revealed that the number of grid cells used is sufficient for accurate modeling of flow for the simulation models in this paper. The input properties used in numerical simulation that are common to all examples are given in Table 3; in Tables 4 and 5, we provide input parameters that vary by example. In Example 1, the hydraulic fracture has infinite conductivity, whereas in Example 2, the hydraulic fracture has finite conductivity. Example 3 uses a homogeneous model, with no stimulated region, and an infinite-conductivity hydraulic fracture. Finally, in Example 4, the hydraulic fracture has infinite conductivity and the stimulated region is assumed to behave as a dual-porosity system. It should be noted that we chose the properties of these examples such that we could observe all possible flow regimes that happen in such reservoirs; therefore, we can observe if the analytical solution is capable of generating accurate forecasts for each flow period.

Fig. 4 compares normalized pressure and its derivative generated with the analytical model and numerical simulation for

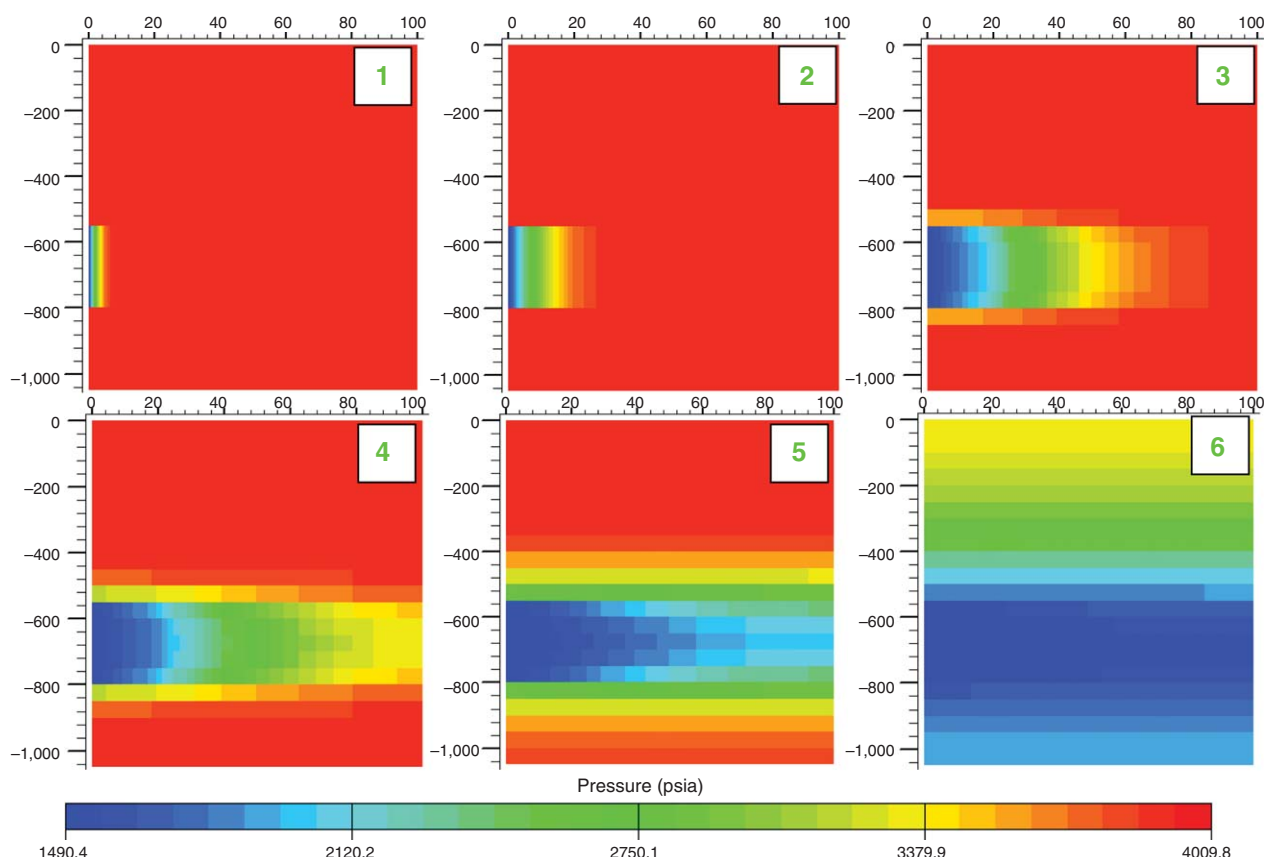


Fig. 5—Pressure-distribution pictures for an arbitrary point in time for each flow period of Example 1. The dimension in the direction parallel to the well has been magnified by 10.

Example 1. Flow periods are specified (numbered from 1 through 6). From the derivative plots, one can identify the flow-regime sequence through time. We also provided pressure-distribution pictures for an arbitrary point in time for each flow period. These pictures, which have been generated with the numerical-simulation model, are presented in Fig. 5. It is noted that the dimension in the direction parallel to well has been magnified by 10 so that pressure distributions can be easily seen. Flow Period 1 corresponds to the presence of transient-linear flow in the stimulated region, characterized by a half-slope line on the derivative. When the pressure response reaches the boundary of stimulated region, the derivative line starts to deviate from the half-slope line. In this period, which is labeled as Period 2, the flow is affected by the boundary of the stimulated region (the boundary parallel to the

fracture). In Period 3, a transient-linear-flow period that is perpendicular to the fracture (parallel to well) develops in the unstimulated zone. In this period, the derivative plot may not develop a perfect half-slope line for two reasons: The linear flow has not completely stabilized yet and/or the unstimulated region beyond the distance penetrated by fracture partially contributes to flow, which promotes formation of radial flow. Period 4 corresponds to the time when flow is dominated by the outer boundary of the unstimulated region (boundary parallel to fracture). After this period, Period 5 represents the formation of a transient-linear flow in the region beyond the area penetrated by the fracture. Note that the direction of this linear flow is parallel to the fracture (perpendicular to well). Finally, in Period 6, flow is dominated by all the outer boundaries. It should be mentioned that all flow periods may not be necessarily observed for various cases. In fact, the geometry of the model dictates the existence of the different flow regimes. For instance, when the ratio of the outer-boundary distance in the x-direction to that in the y-direction is small, we may not observe Flow Periods 4 and 5. Further, for very-low-permeability reservoirs, we may never observe the late-flow periods because the production rate may reach economic limit before the entire reservoir has been completely drained. A more-thorough discussion of these flow periods is presented later in this study.

In Figs. 6 and 7, Examples 2 and 3, are shown, respectively, for comparison. In Example 2, the same flow periods are present as in Example 1, except we also observe fracture-linear flow and fracture-bilinear-flow regimes at early time. This is because the fracture has finite conductivity in this example. In Example 3, the same flow periods as those of Example 1 are again observed, except for the first linear-flow and boundary-dominated-flow periods (because there is no stimulated region for this example).

We also created an example in which the stimulated region behaves as a dual-porosity system (Example 4). The properties specific to this example are presented in Table 5. A comparison of numerical and analytical simulation is provided in Fig. 8. In Fig.

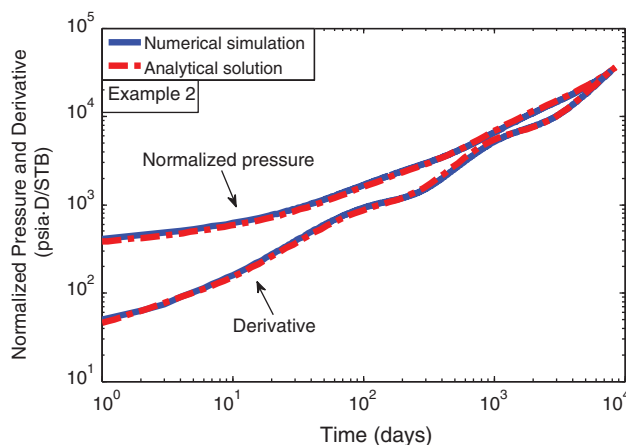


Fig. 6—Comparison of numerical simulation and analytical solution: Example 2.

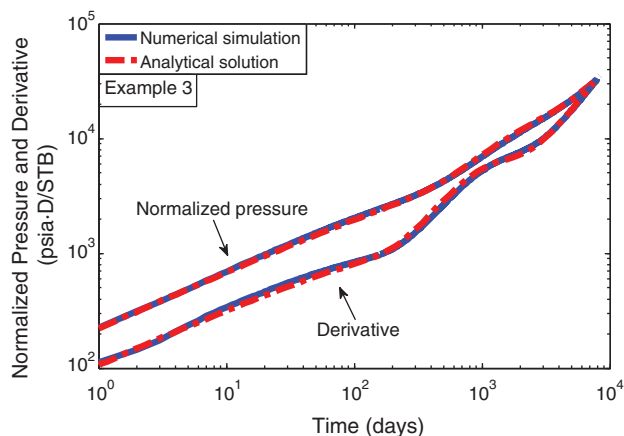


Fig. 7—Comparison of numerical simulation and analytical solution: Example 3.

8, in addition to the mentioned flow periods in Example 1, we observe a valley-shaped period, which is a signature of naturally fractured reservoirs when using the pseudosteady-state model to represent the matrix. In this example, this valley-shaped period has distorted the ending of the first linear-flow period and early part of the first boundary-dominated-flow period. As Figs. 4, 6, 7, and 8 illustrate, the analytical solution is in excellent agreement with numerical simulation. It is also observed that the analytical solution can accurately reproduce different flow regimes.

As mentioned previously, the presented model is more general than the trilinear-flow model (Brown et al. 2011) and the enhanced-fracture region (EFR) model (Stalgorova and Mattar 2013). Note that the new solutions may not exhibit excellent accuracy when all the following conditions are met: y_{De} is very large, y_{De} is nearly equal or greater than x_{D1} , and value of y_{Ds} is in a moderate range (not small and not large compared with y_{De}). If one of the mentioned conditions is violated, accuracy of the solutions increases. However, even in this range the presented solutions are still more accurate than those of the previous EFR model. Further, the dimensions of real multifracted horizontal wells typically are in a range for which the new solutions are accurate. We have provided a comparison between the new EFR model developed in this paper and the previous EFR model in Appendix E to demonstrate the greater accuracy of the former. We have also provided a discussion about the range of validity of the presented solutions in Appendix E.

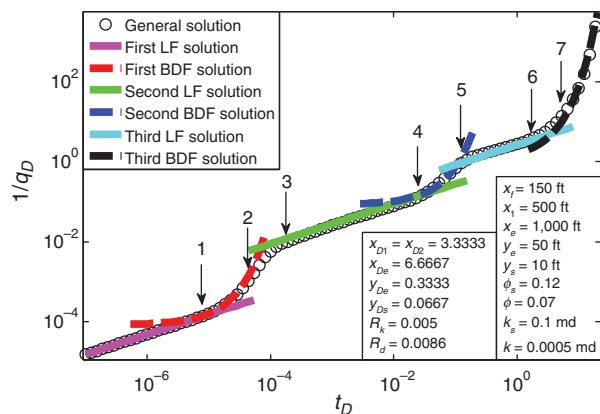


Fig. 9—Comparison of general solution and local solutions: Point 1 is end of the first LF period and start of the first BDF period; Point 2 is end of the first BDF period; Point 3 is start of the second LF; Point 4 is end of the second LF period and start of the second BDF period; Point 5 is end of the second BDF and start of the third LF period; Point 6 is end of the third LF period; and Point 7 is start of the third BDF period.

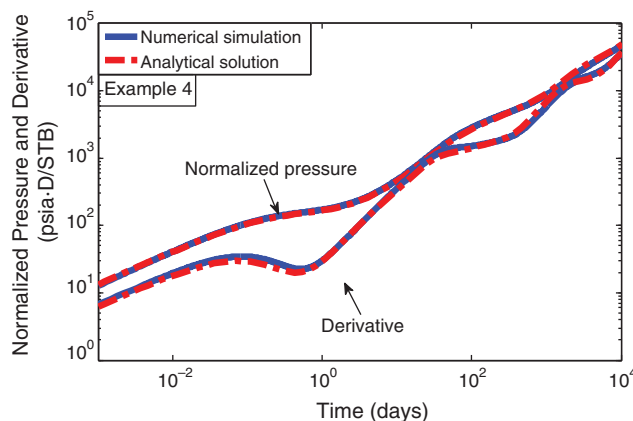


Fig. 8—Comparison of numerical simulation and analytical solution: Example 4 (stimulated region is dual porosity).

Flow-Regime Sequence and Local (Flow-Regime-Specific) Solutions

In multifracted horizontal wells, with an enhanced fracture region, we may observe several flow regimes. These flow regimes are: fracture linear flow (LF), bilinear flow, first LF, first boundary-dominated flow (BDF), second LF, second BDF, third LF, and third BDF. The fracture LF and bilinear-flow regimes are not commonly observed with field data. The successive flow regimes can be seen in Fig. 9, in which the general (full) analytical solution and local solutions (flow-regime-specific solutions) are plotted for an example. The first LF occurs in the stimulated region for the period before the boundary of this region experiences a pressure drop. Once the pressure pulse reaches the boundary of the stimulated zone, the first BDF regime is observed. Note that this boundary is parallel to fracture and located at distance Y_s (Fig. 2). After a transition time, a LF period that is perpendicular to the fracture (parallel to well) develops in the unstimulated zone. This is the second LF period. After another transition period, the pressure response is dominated by the boundary of the unstimulated zone, which is parallel to the fracture and located at distance Y_e (Fig. 2). This is the second BDF period. The third LF period is formed in the region beyond the distance penetrated by fracture. Finally, the third BDF regime occurs when the boundaries at the distances of X_1 and X_2 experience a pressure drop. It should be considered that the transitions between flow regimes may sometimes completely mask a flow regime so that we may not necessarily observe all flow periods. Depending on the dimensions and properties of the system, some of the flow regimes may not actually occur. In addition, we may not observe late-flow periods because the rate may reach its economic limit before they can occur. In shale plays, which have very-low permeability, we observe early-flow regimes (first and second LF regimes), whereas in tight-gas systems, which have higher conductivity, we may not see the early-flow regimes but can observe late-flow periods such as third LF.

We can use local solutions to analyze each flow regime. The solutions for transient LF and boundary-dominated LF for constant-pressure production in a linear system were reported by Arevalo-Villagran and Wattenbarger (2001). The solution for constant-rate production from an infinite-conductivity fracture for BDF occurring in a rectangular system was reported by Gringarten et al. (1974). For constant-pressure production, the BDF solution is different. We have adapted these solutions for each flow regime in our system, as presented in Table 6.

Fig. 9 presents an example in which the general (full) analytical solution and local solutions are plotted. The dimensions and properties of this example are selected such that all flow regimes can be observed. The start and end of each flow regime is specified by use of numbers in Fig. 9. Note that for the situation where fracture completely penetrates the formation in the x -direction, or where the permeability of the region beyond the penetration

Sequence of Flow Regimes	Relation
First LF	$\frac{1}{q_D} = \frac{R_k}{2} \sqrt{\frac{\pi t_D}{R_\eta}}$
First BDF	$\frac{1}{q_D} = \frac{R_k y_{Ds}}{4} \exp\left(\frac{\pi^2 t_D}{4 R_\eta y_{Ds}^2}\right)$
Second LF	$\frac{1}{q_D} = \frac{1}{2} \sqrt{\pi t_D}$
Second BDF	$\frac{1}{q_D} = \frac{y_{De}}{4} \exp\left(\frac{\pi^2 t_D}{4 y_{De}^2}\right)$
Third LF	$\frac{1}{q_D} = \frac{1}{2} \sqrt{\frac{\pi t_D}{y_{De}^2}}$
Third BDF	$\frac{1}{q_D} = \frac{1}{\pi} \ln\left(4 \sqrt{\frac{2 y_{De} x_{De}}{C_A e^\gamma}}\right) \exp\left[\frac{2 \pi t_D}{2 y_{De} x_{De} \ln\left(4 \sqrt{\frac{2 y_{De} x_{De}}{C_A e^\gamma}}\right)}\right]$

Table 6—Flow regimes and their solutions.

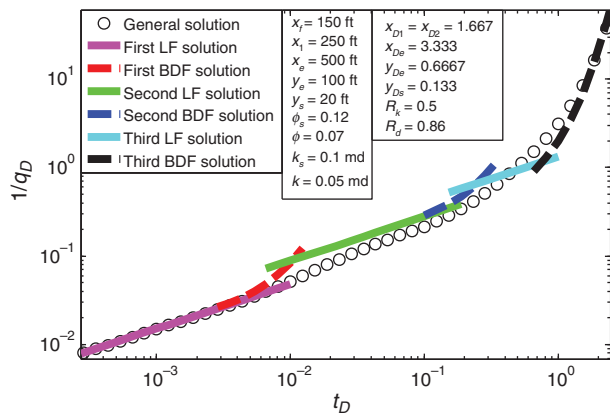


Fig. 10—Comparison of general solution and local solutions.

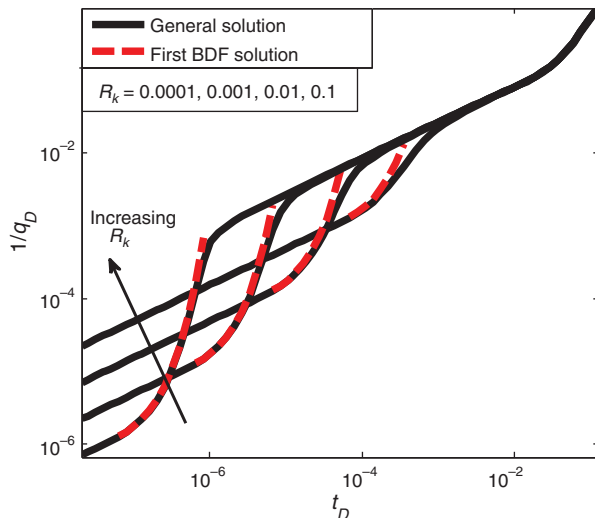


Fig. 11—Effect of ratio of permeability of the unstimulated zone to permeability of stimulated zone (R_k).

x_{De}	5.0
x_{D1}	2.5
x_{D2}	2.5
y_{De}	0.3
y_{Ds}	0.03
R_k	0.005
R_ϕ	0.3

Table 7—Base-case data for sensitivity studies.

distance of the fracture is extremely low, the third LF and third BDF periods would not occur. As mentioned, we may not necessarily see all flow regimes.

In Fig. 10, we present another example in which only the first LF and third BDF periods appear. This example is given to show that we cannot always predict or analyze flow behavior of such systems by use of simple local solutions; this is because to extract quantitative information from the flow regime, we must understand what the flow geometry is.

Sensitivity Studies

Depending on the geometry and properties of the system, we may observe different flow characteristics. In the following, we investigate the effect of different parameters on the rate-transient response of systems with an enhanced fracture region. The dimensionless parameters for the base case are given in Table 7.

The effect of the ratio of permeability of the unstimulated zone to permeability of stimulated zone (R_k) is presented in Fig. 11. In Fig. 11, the first and second linear-flow (LF) and boundary-dominated-flow (BDF) periods are depicted. As R_k increases, duration of the first LF period increases, whereas duration of the second LF period decreases. Note that an increase in R_k is equivalent to a decrease in permeability of the stimulated region and/or increase in permeability of the unstimulated region. Accordingly, when permeability of the stimulated region decreases, the pressure response travels slower and the effect of the first boundary is felt later. In the same way, when the permeability of the unstimulated region increases, the pressure pulse reaches the second boundary faster and that is why the second LF period is shortened. For high values

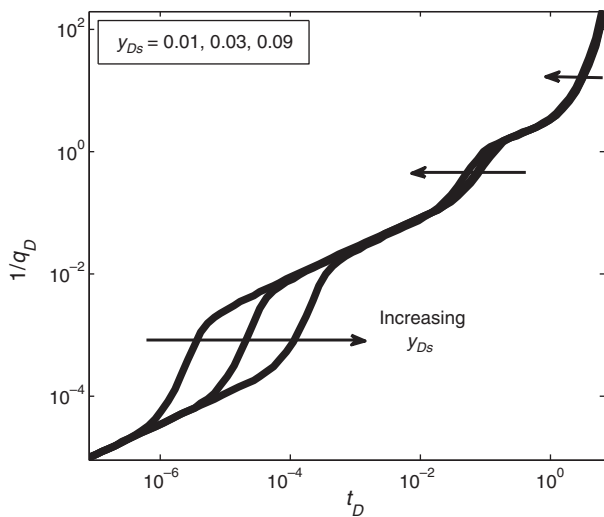


Fig. 12—Effect of size of the stimulated zone (y_{Ds}).

of R_k , where permeability of the stimulated zone is not much higher than that of the unstimulated zone, the second LF period may be completely masked. In this case, we may see the second BDF period after the first BDF period, with a transition period in between. It is also observed that, for low values of R_k , the first BDF solution (given in Table 7) can be used for simulating or analysis of the first BDF period. As the value of R_k approaches unity, the first BDF solution is unable to match the first BDF period. This is because the first BDF solution was originally developed for a sealed boundary. For a very-sharp contrast in permeability of the stimulated and unstimulated regions, the first boundary behaves as a sealed boundary until the pressure drop across the boundary becomes large enough to allow fluid to flow from the unstimulated region into the stimulated region. When such fluid transfer starts across this boundary, the first BDF solution is no longer applicable. As R_k increases, the permeability contrast decreases; therefore, with increasing R_k we observe a shorter time period during which there is no fluid transfer across the boundary. It is further observed that variations in R_k do not affect the second BDF period and later flow periods. In summary, as the permeability of the stimulated zone decreases, the accuracy of the first BDF solution decreases and the second LF period tends to be shorter or does not occur.

The effect of size of the stimulated zone (y_{Ds}) is illustrated in Fig. 12. As can be observed, increasing y_{Ds} does not affect the

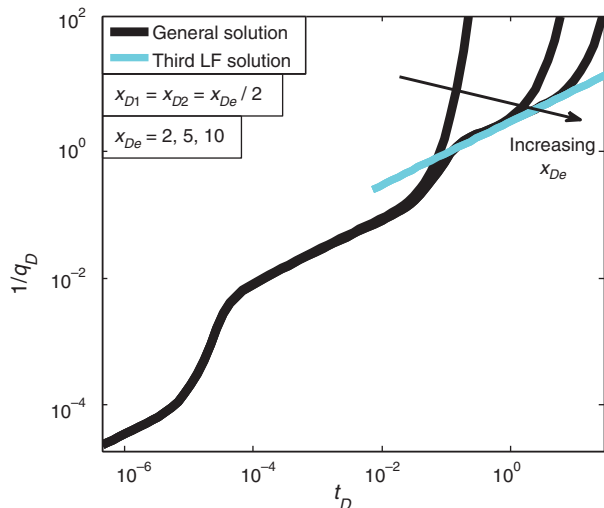


Fig. 14—Effect of distance from the well to the outer boundary in x -direction (x_{De}).

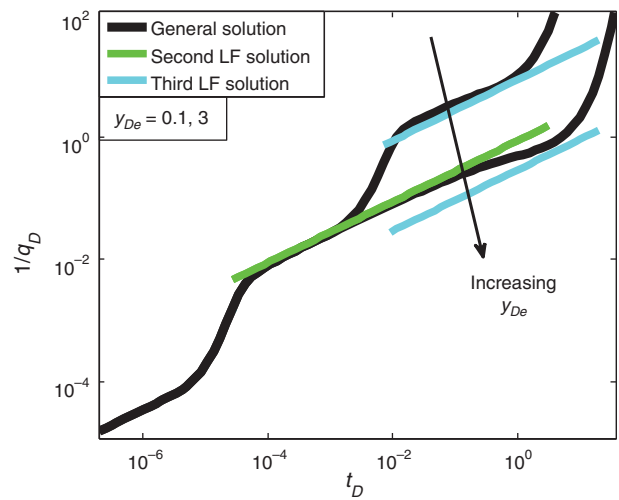


Fig. 13—Effect of fracture half-spacing (y_{De}).

shape of the first BDF period; it only shifts this period to the right. The reason for this is that the shape of the first BDF period is mainly dependent on the permeability contrast (R_k) of the stimulated and unstimulated regions, which is kept constant for all cases in Fig. 12. Clearly, as y_{Ds} increases, the time for when the pressure pulse reaches the boundary of the stimulated region increases, and that is why we observe that for higher values of y_{Ds} , the duration of the first LF period increases. However, increasing y_{Ds} shifts the second and third BDF periods to the left. In another words, when increasing the stimulated distance, the pressure response reaches the boundary of the stimulated zone later, but reaches the corresponding boundaries of the second and third BDF period sooner because of the higher permeability of stimulated zone (relative to the unstimulated zone).

Fig. 13 illustrates the effect of fracture spacing in y -direction (y_{De}). As Fig. 13 demonstrates, for higher values of y_{De} , the duration of the second LF increases and the forecast tends to deviate below the LF line later in time. This deviation is caused by the switch of the flow regime from linear to pseudoradial flow. For systems with an enhanced-fracture region, the probability of seeing pseudoradial flow is quite low. This is because fracture spacing in multifracted horizontal wells (MFHWs) is not usually large enough to allow the formation of the pseudoradial-flow regime. In Fig. 13, the second and third LF solutions are also depicted; as can be observed, increasing y_{De} shifts the third LF period downward. For this specific example, we see that for $y_{De} = 3$, the pressure response reaches the outer boundary (x_{De}) before the third LF period is fully developed. If the distance from the well to the boundary in the x -direction (x_{De}) is large enough, the forecast would exhibit the third LF period instead of the third BDF regime.

In Fig. 14, the impact of distance from the well to the outer boundary in the x -direction (x_{De}) is illustrated. The fracture is centered between the two boundaries in the x -direction ($x_{D1} = x_{D2} = x_{De}/2$) for this specific example. As x_{De} increases, the duration of the third LF period increases and development of the third BDF period is delayed. Because the third LF period corresponds to the transient-pressure pulse traveling in the region beyond the area penetrated by fracture, by increasing x_{D1} (the distance between tips of fracture and outer boundary), the duration of this transient-flow period increases and the time when the pressure pulse reaches the outer boundary is delayed. In Fig. 14, the first BDF stem corresponds to the case when the fracture completely penetrates the reservoir in the x -direction. In this case we do not observe third LF and BDF periods.

As mentioned previously, local solutions may not always match the corresponding flow periods observable in the general solution. Here, we attempt to match the local solution for the second BDF period to the second BDF period of the general solution.

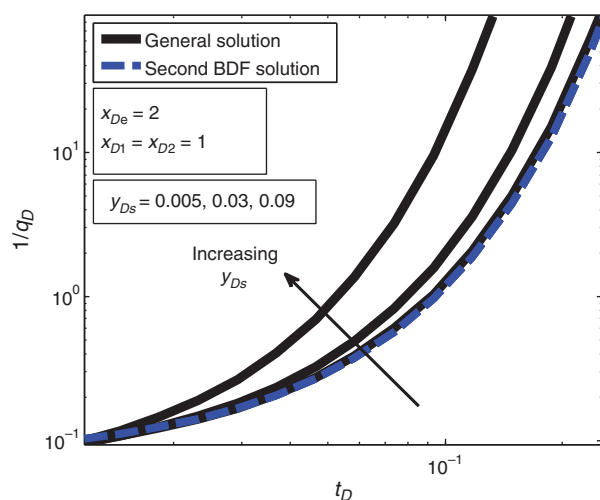


Fig. 15—Effect of y_{Ds} on the accuracy of second BDF solution for matching second BDF period.

Two parameters, which are y_{Ds} and y_{De} , affect this flow period. The effect of y_{Ds} is illustrated in **Fig. 15**. We observe that for very-small values of y_{Ds} , the second BDF (local) solution matches this period but as y_{Ds} increases, the flow period shifts to the left and the local solution is no longer applicable. This is because the second BDF solution was originally developed for a homogeneous system, but here we are dealing with a composite system. For small values of y_{Ds} where the size of the stimulated region is much smaller than the size of the virgin zone, the system can be approximated by a homogeneous system with the permeability of the virgin zone. However, as the size of the stimulated region increases, it cannot be ignored and that is why for higher values of y_{Ds} , the second BDF solution is not applicable. For such systems, the second BDF solution should be modified for composite systems. Note that **Fig. 15** corresponds to the case where the hydraulic fracture completely penetrates the formation in the x -direction. **Fig. 16** presents the effect of y_{De} on the local-solution match. As y_{De} increases, the accuracy of the second BDF local solution decreases. The reason behind this observation is that as y_{De} increases, the contribution of the region beyond the interfracture area is increased, and therefore when the pressure pulse reaches the second boundary, the transients from the area beyond the interfracture region become significant enough to prevent the formation of a pure BDF period. We observe that the local solution

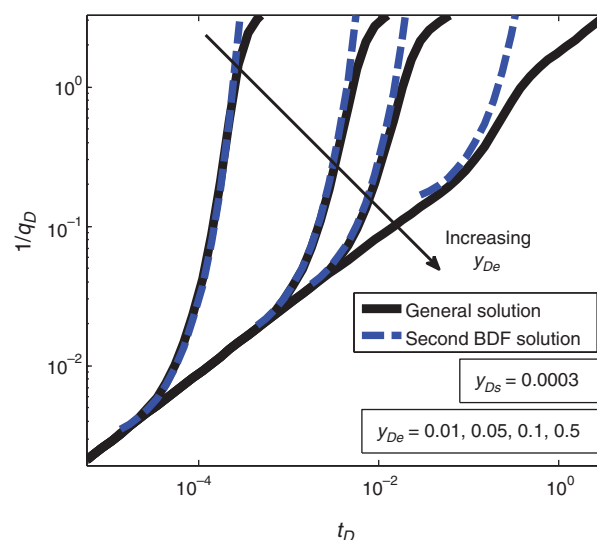


Fig. 16—Effect of y_{De} on the accuracy of second BDF solution for matching second BDF period.

is applicable only for small values of y_{De} . If, for example, we consider $y_{De} = 0.1$ to be the limit for which the second BDF solution is valid, we can use this solution only for cases where fracture length is at least 10 times greater than fracture spacing. This may be a rare case when dealing with real MFHWs. Therefore, analyzing the second BDF period with the use of conventional BDF equations is problematic unless the flow is dominated by all four boundaries. Under two situations we can interpret BDF data by use of the conventional equations: First, the boundaries in x -direction must be close enough to the tips of the fracture so that transient flow from the region beyond the interfracture region is short-lived and can be ignored; and second, if transient flow from the region beyond the interfracture region cannot be ignored, enough time should pass so that the third BDF is established.

Discussion: Production Analysis of Shale Plays With Enhanced-Fracture Region (EFR)

As noted previously, we may not observe all the flow regimes illustrated so far in this study with our new EFR model in field-production data. In shale reservoirs, which have extremely low matrix permeability, it is possible that boundary-dominated flow (BDF) is not observed after several years of production. Although the development of EFR in these reservoirs may improve production, the first and second linear-flow (LF) periods may last for several years because of very-low permeability of the unstimulated zone. In systems with higher matrix permeability, however, later flow periods such as the third flow periods may be observable during early stages of production. In the following, we extend our discussion to practical issues related to the application of the new EFR model to field cases.

Here we limit our discussion to the first and second LF periods, which are expected to be dominant at early stages of production from shale plays. For simplicity, we assume that the fracture completely extends to the boundaries in x -direction ($x_{De} = 2$), which is commonly assumed in the literature (Ozkan et al. 2011). To illustrate production responses of the EFR system in this case, we prepared a synthetic example in which the well is maintained at constant pressure and is labeled as CP. In this example, the fracture is assumed to have infinite conductivity. The properties of this example are $x_f = 200$ ft, $x_e = 400$ ft, $y_s = 25$ ft, $y_e = 150$ ft, $k = 0.0001$ md, and $k_s = 0.001$ md. Other properties are the same as those in Table 3. The production response of this example on a log-log plot is presented in **Fig. 17**; we observe two half-slope straight regions, which correspond to the first and second LF periods, and a transition period that reflects the influence of the boundary of the stimulated zone. The half-slope regions of the

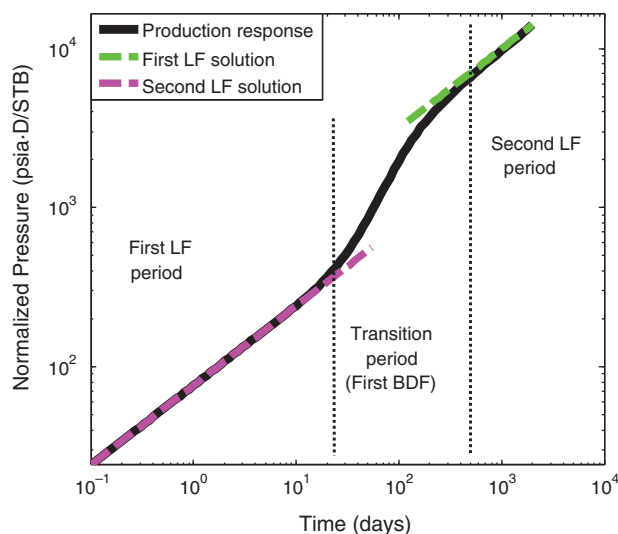


Fig. 17—Production response and flow periods of the synthetic CP example in a log-log plot.

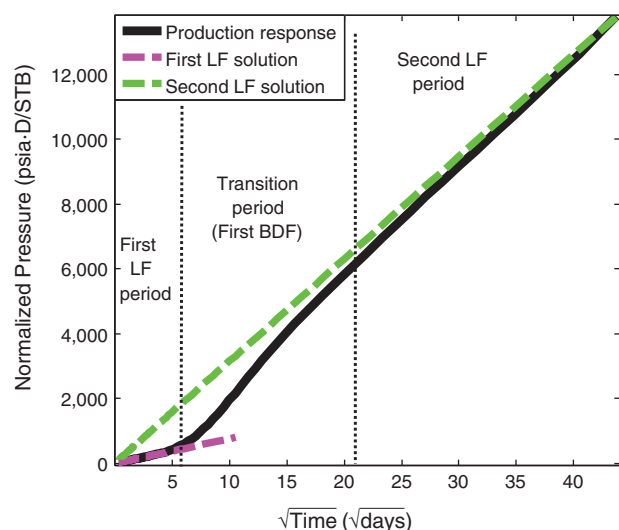


Fig. 18—Production response and flow periods of the synthetic CP example in a square-root-of-time plot.

plot are matched with first and second LF (local) solutions. Note that the second half-slope line appears above the first one. If such behavior is observed in field data, it could be indicative of the presence of EFR around the fractures. **Fig. 18** presents the square-root-of-time plot for this example. The first and second LF periods and transition period are observable. The local (straight-line) solutions corresponding to the first and second LF periods are also depicted. The first LF solution exhibits an excellent match to the first LF period of the general solution. The second LF local solution does not exactly match the general solution, but approaches it at late time (i.e., the general solution exhibits straight-line behavior only at late time for the second LF period). To match the second LF period on a square-root-of-time plot, a line is plotted through the origin and through the data at late time, which exhibit straight-line behavior. Importantly, the transition period on the square-root-of-time plot also exhibits a near straight-line trend; if a line were incorrectly fitted to this transition period, assuming it was LF, it would exhibit a negative intercept. This is illustrated in **Fig. 19**. The apparent straight-line trend after the first LF period can mislead the analyst, who may guess that this linear trend on the square-root-of-time plot is the signature of the second LF period when in fact it is not. When field data plotted on a square-root-of-time plot exhibit a linear trend with a negative intercept, it could signify the presence of a stimulated region near the hydraulic

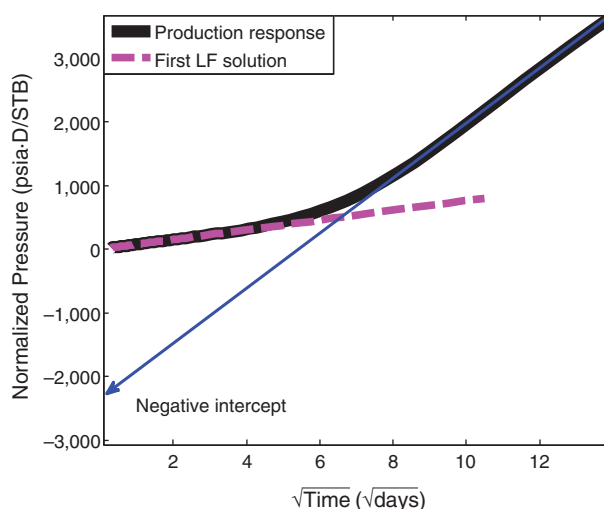


Fig. 19—Observation of negative intercept in the square-root-of-time plot of the synthetic CP example from the line fitted to the straight part of transition period.

fractures; however, the negative intercept also indicates that the trend should not be interpreted as the second LF period, and analysis of this (transitional) flow period for hydraulic-fracture properties could be in significant error. As mentioned previously, the line fit to the second LF period must pass through the origin of the square-root-of-time plot.

We caution, however, that the negative intercept does not necessarily indicate the presence of EFR; EFR is only one possible cause of the negative intercept on square-root-of-time plots. We emphasize that our previous statements are valid for constant pressure production, which is often the dominant production mode in very-low-permeability reservoirs. However, in the early period of production, flowing bottomhole pressure (BHP) may decline until a limit is reached, and thereafter remains relatively constant. We prepared another synthetic example with the same reservoir properties as the previous case, but the production rate is set to a constant value during early time, after which the well switches to constant-pressure mode. The production rates for this example are shown in **Fig. 20**. A log-log plot of normalized pressure vs. time for the previous and current examples (labeled as CP and CR+CP, respectively) is given in **Fig. 21**. As seen, the first LF local solution for constant rate matches the early simulated CR+CP data because the well is produced at a

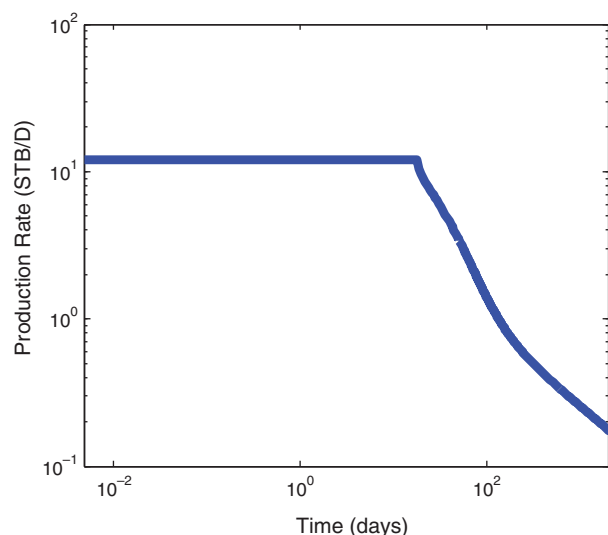


Fig. 20—Production rate for the synthetic CR+CP example.

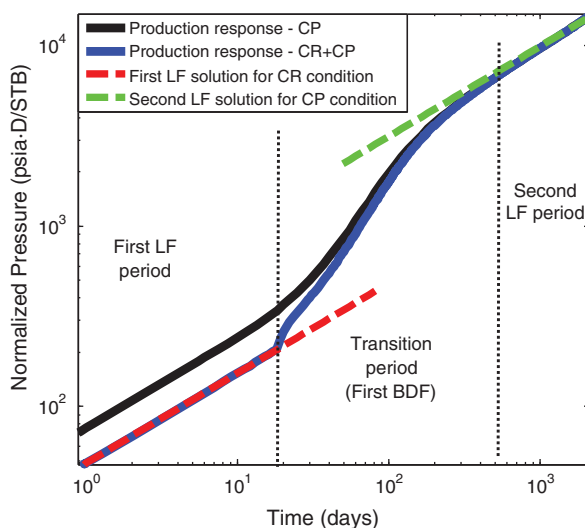


Fig. 21—Comparison of log-log production response and flow periods of CP and CR+CP examples.

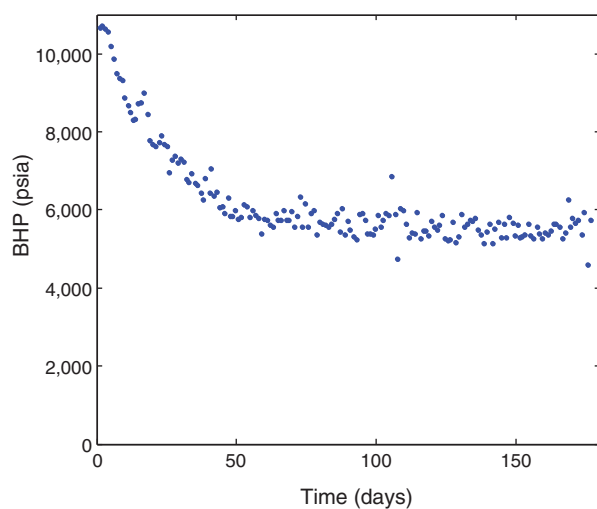


Fig. 22—BHP data of the field example.

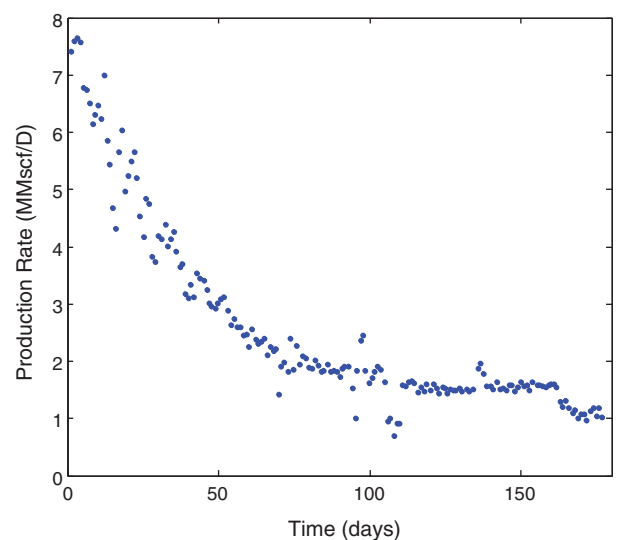


Fig. 23—Production-rate data of the field example.

constant rate during this period. An important observation is that the second LF CP local solution matches the late simulated CR+CP data regardless of the fact that the well was produced at constant rate during the early days of production. However, a good practice while using local (straight-line) solutions is to use superposition time combined with normalized rate to convert data to an equivalent constant-rate solution; this is because real data may not exhibit either pure constant-rate or pure constant-flowing-pressure production.

We illustrate some of these issues with a real field example. The production data of this example, which are presented in Figs. 22 and 23, were extracted from the paper by Stalgorova and Mat-tar (2012). We see that the BHP declines during early days of production, and then remains relatively constant during the late period. The normalized pseudopressure data were also extracted from the same paper. These data were recently reanalyzed by the authors to demonstrate the application of a simplified EFR model (Clarkson et al. 2014). Accordingly, here we do not perform quantitative analysis of these data and only provide a few qualitative remarks.

As discussed by Clarkson (2013) and further illustrated by Clarkson et al. (2014), the first step in quantitative analysis of production data, after data review and quality control, is the identification of flow regimes. This may be achieved by use of a

combination of log-log diagnostic plots and specialty (e.g., Cartesian and square-root-of-time) plots, as illustrated by Clarkson et al. (2014) previously for this example. For the simulated cases provided previously, the product of kx_f can be estimated from the slope of square-root-of-time data for the first and second LF periods; further, the size of the stimulated zone can be determined from the equation of distance of investigation. The current field example appears to exhibit behavior similar to the second synthetic (CP+CR) example provided previously. Fig. 24 presents the log-log plot of normalized pseudopressure vs. time for this example; we see that the first and second LF periods can be distinguished by use of half-slope lines and the transition period is observed between these LF periods (similar to Fig. 21). The square-root-of-time plot of this example is also shown in Fig. 25, in which flow periods are specified. As explained previously for the synthetic example, the second LF period is analyzed by fitting a line passing through the origin on one end and through data coinciding with the second LF period on the other end. Although the well pressure is not constant at early days of production, it becomes constant for middle to late times. Therefore, the constant-pressure solution can be used to analyze the second LF period. One can also apply linear superposition time to use the constant-rate solution to analyze this period, as did Clarkson et al.

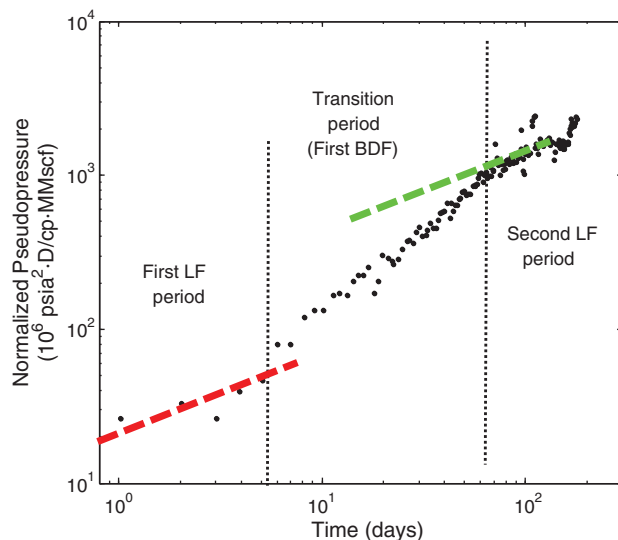


Fig. 24—Log-log production response and flow periods for the field example.

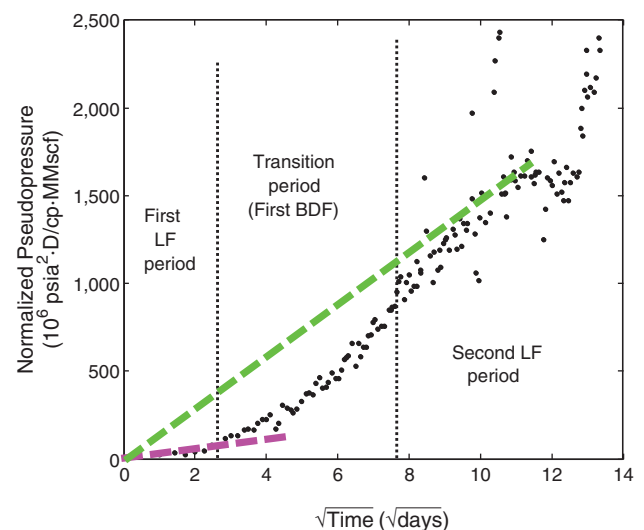


Fig. 25—Production response and flow periods for the field example in a square-root-of-time plot.

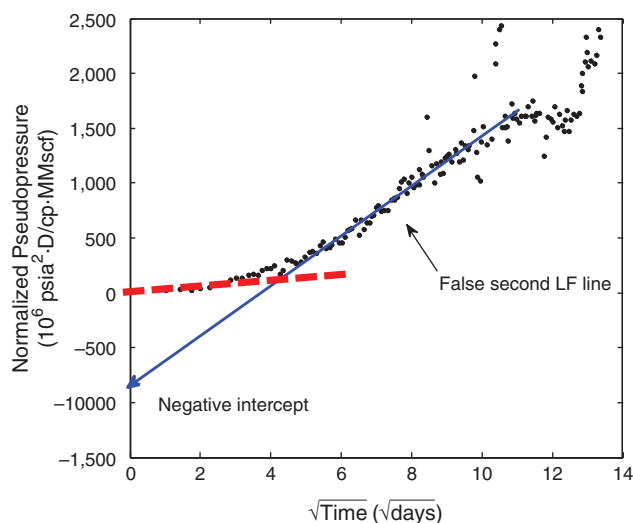


Fig. 26—Observation of negative intercept in the square-root-of-time plot of the field example.

(2014). In Fig. 26, a straight line is also fitted to both transition and second LF periods and exhibits a negative intercept. As noted previously for the synthetic example, this negative intercept indicates the presence of EFR near the hydraulic fracture. However, with reference to the line in Fig. 26, if we assume (falsely) that the straight-line fit through the transition period is pure LF corresponding to the second LF period, we could derive incorrect ($\sqrt{kx_f}$) information from the slope of this line. The correct line for analysis of the second LF period is shown in Fig. 25. From the slope of this line, one can derive true information.

Conclusions

In this work, we have provided a fully analytical model for analyzing and forecasting multifractured horizontal wells (MFHWs) exhibiting complex fracture geometry that is more general and flexible than analytical solutions provided to date. We demonstrate the flexibility of the new model by showing the full range of sequence of flow regimes that the model is capable of generating and performing a sensitivity study by use of different model geometries. The solutions are very accurate for a wide range of reservoir parameters. However, solution accuracy reduces when all the following conditions are met: y_{De} is very large, y_{De} is nearly equal to or greater than x_{D1} , and the value of y_{Ds} is in a moderate range (not small and not large compared with y_{De}). If one of the mentioned conditions is violated, the accuracy of solutions increases. It should be noted, however, that the model is accurate for typical dimensions observed for real MFHWs.

We further provide local solutions that can be used to analyze each individual flow regime. Very importantly, we highlight the practical issue that local (or straight-line) solutions used in isolation can yield incorrect information about the reservoir/fracture. For example, straight-line behavior is often observed on a square-root-of-time plot when analyzing MFHWs, which is commonly used to analyze transient linear flow (LF). In some cases, a straight-line fit to data on this plot may yield a negative intercept; we demonstrate, by use of our new enhanced-fracture-region (EFR) model, that this negative intercept may indicate EFR behavior, but the straight line should not be interpreted as LF, but rather as transitional flow between two LF periods. Other issues of practical importance that can be addressed with the new model are also highlighted.

Nomenclature

- a_1 = a solution parameter defined in Table 2, dimensionless
- a_2 = a solution parameter defined in Table 2, dimensionless
- a_3 = a solution parameter defined in Table 2, dimensionless
- a_4 = a solution parameter defined in Table 2, dimensionless

- a_5 = a solution parameter defined in Table 2, dimensionless
- a_6 = a solution parameter defined in Table 2, dimensionless
- a_7 = a solution parameter defined in Table 2, dimensionless
- B = formation volume factor, bbl/STB
- c_t = total compressibility, 1/psia
- C_A = pseudosteady-state-shape factor, dimensionless
- F_{CD} = dimensionless conductivity defined in Table 1, dimensionless
- F_{CDs} = dimensionless conductivity defined in Table 1, dimensionless
- h = formation thickness, ft
- k = permeability, md
- n = Fourier-transform variable, dimensionless
- p = pressure, psia
- q = flow rate, STB/d
- r_w = wellbore radius, ft
- R_η = diffusivity ratio defined in Table 1, dimensionless
- R_k = permeability ratio defined in Table 1, dimensionless
- $R_{\eta f}$ = diffusivity ratio defined in Table 1, dimensionless
- s = Laplace variable, dimensionless
- S_c = convergence skin, dimensionless
- S_w = initial water saturation, dimensionless
- t = time, day
- w = fracture opening, ft
- x = x -distance (coordinate), ft
- x_f = fracture half-length, ft
- y = y -distance (coordinate), ft
- y_e = fracture half-spacing, ft
- η = hydraulic diffusivity, md,psia/cp
- θ = θ -direction (coordinate), ft
- λ = matrix-fracture transfer parameter defined by Eq. 24, dimensionless
- μ = viscosity, cp
- ξ_n = Fourier parameter defined by Eq. C-13, dimensionless
- σ = shape factor, 1/ft²
- ϕ = porosity, dimensionless
- ω = storage ratio, dimensionless

Subscripts

- ave = average
- cp = constant pressure
- cr = constant rate
- C = presence of convergence
- CS = convergence skin
- D = dimensionless
- e = external boundary
- f = fracture
- i = initial
- L = linear
- m = matrix
- S = stimulated region
- u = unit rate
- w = well flow
- 1 = Region 1
- 2 = Region 2
- 3 = Region 3
- 1s = interface of Region 1 and stimulated region

Superscripts

- \sim = Laplace-transform operator
- \sim = Fourier-transform operator

Acknowledgments

The authors would like to thank ConocoPhillips for supporting this research. In particular, we would like to thank George Petrosky for his helpful discussions on the topic of “negative intercepts.” Author C. R. Clarkson would like to thank Shell, Encana, and Alberta Innovates Technology Solutions for supporting his position as Chair in Unconventional Gas and Light Oil Research, Department of Geoscience, University of Calgary.

References

- Arevalo-Villagran, J. A. and Wattenbarger, R. A. 2001. Long-Term Linear Flow in Tight Gas Wells. Technical report, Texas A&M University, College Station, Texas, March 2001.
- Brown, M., Ozkan, E., Raghavan, R., et al. 2011. Practical Solutions for Pressure-Transient Responses of Fractured Horizontal Wells in Unconventional Shale Reservoirs. *SPE Res Eval & Eng* **14** (6): 663–676. SPE-125043-PA. <http://dx.doi.org/10.2118/125043-PA>.
- Clarkson, C. R. 2013. Production Data Analysis of Unconventional Gas Wells: Workflow. *Int. J. Coal Geol.* **109–110** (1 April): 147–157. <http://dx.doi.org/10.1016/j.coal.2012.11.016>.
- Clarkson, C. R., Williams-Kovacs, J. D., Qanbari, F., et al. 2014. History-Matching and Forecasting Tight/Shale Gas Condensate Wells Using Combined Analytical, Semi-Analytical, and Empirical Methods. Presented at the SPE/CSUR Unconventional Resources Conference – Canada, Calgary, Alberta, Canada, 30 September–2 October. SPE-171593-MS. <http://dx.doi.org/10.2118/171593-MS>.
- de Swaan O., A. 1976. Analytical Solutions for Determining Naturally Fractured Reservoir Properties by Well Testing. *SPE J.* **16** (3): 117–122. SPE-5346-PA. <http://dx.doi.org/10.2118/5346-PA>.
- Gringarten, A. C., Ramey, H. J. and Raghavan, R. 1974. Unsteady-State Pressure Distributions Created by a Well With a Single Infinite-Conductivity Vertical Fracture. *SPE J.* **14** (4): 347–360. SPE-4051-PA. <http://dx.doi.org/10.2118/4051-PA>.
- Mukherjee, H. and Economides, M. J. 1991. A Parametric Comparison of Horizontal and Vertical Well Performance. *SPE Form Eval* **6** (2): 209–216. SPE-18303-PA. <http://dx.doi.org/10.2118/18303-PA>.
- Odeh, A. S. 1968. Steady-State Flow Capacity of Wells With Limited Entry to Flow. *SPE J.* **8** (1): 43–51. SPE-1797-PA. <http://dx.doi.org/10.2118/1797-PA>.
- Ozkan, E., Brown, M., Raghavan, R., et al. 2011. Comparison of Fractured-Horizontal-Well Performance in Tight Sand and Shale Reservoirs. *SPE Res Eval & Eng* **14** (2): 248–259. SPE-121290-PA. <http://dx.doi.org/10.2118/121290-PA>.
- Samandari, O., McDonald, B., Barzola, G., et al. 2014. Understanding Shale Performance: Performance Analysis Workflow with Analytical Models in Eagle Ford Shale Play. Presented at the SPE Unconventional Resources Conference, The Woodlands, Texas, 1–3 April. SPE-169004-MS. <http://dx.doi.org/10.2118/169004-MS>.
- Stalgorova, E. and Mattar, L. 2012. Practical Analytical Model to Simulate Production of Horizontal Wells with Branch Fractures. Presented at the SPE Canadian Unconventional Resources Conference, Calgary, Alberta, Canada, 30 October–1 November. SPE-162515-MS. <http://dx.doi.org/10.2118/162515-MS>.
- Stalgorova, E. and Mattar, L. 2013. Analytical Model for Unconventional Multifractured Composite Systems. *SPE Res Eval & Eng* **6** (3): 246–256. SPE-162516-PA. <http://dx.doi.org/10.2118/162516-PA>.
- van Everdingen, A. F. and Hurst, W. 1949. The Application of the Laplace Transformation to Flow Problems in Reservoirs. *J Pet Technol* **1** (12): 305–324. SPE-949305-G. <http://dx.doi.org/10.2118/949305-G>.
- Warren, J. E. and Root, P. J. 1963. The Behavior of Naturally Fractured Reservoirs. *SPE J.* **3** (3): 245–255. SPE-426-PA. <http://dx.doi.org/10.2118/426-PA>.

Appendix A—Derivation of Solution for Production Rate: Infinite-Conductivity-Fracture Case

In the following, the rate produced from an infinite-conductivity fracture with constant pressure in a rectangular composite reservoir is derived. The placement of the hydraulic fracture coincides with the line of symmetry.

The nomenclature for dimensions of the system is presented in Fig. 2. Fig. 3 shows different regions of the physical system. By use of the dimensionless variables of Table 1, the differential equation and boundary conditions in Laplace space for Region 2 are

$$\frac{\partial^2 \bar{p}_{D2}}{\partial x_D^2} - s\bar{p}_{D2} = 0, \quad \dots \quad (\text{A-1})$$

$$\frac{\partial \bar{p}_{D2}}{\partial x_D} = 0, \quad x_D = 0, \quad \dots \quad (\text{A-2})$$

$$\bar{p}_{D2} = \bar{p}_{Ds}, \quad x_D = x_{D1} - 1. \quad \dots \quad (\text{A-3})$$

The solution in Laplace space for Region 2 is obtained as

$$\bar{p}_{D2} = \frac{\bar{p}_{Ds}}{\cosh[\sqrt{s}(x_{D1} - 1)]} \cosh(\sqrt{s}x_D). \quad \dots \quad (\text{A-4})$$

The differential equation and boundary conditions in Laplace space for Region 3 are written as

$$\frac{\partial^2 \bar{p}_{D3}}{\partial \theta_D^2} - s\bar{p}_{D3} = 0, \quad \dots \quad (\text{A-5})$$

$$\frac{\partial \bar{p}_{D3}}{\partial \theta_D} = 0, \quad \theta_D = 0, \quad \dots \quad (\text{A-6})$$

$$\bar{p}_{D3} = \bar{p}_{Ds}, \quad \theta_D = x_{D2} - 1. \quad \dots \quad (\text{A-7})$$

The solution in Laplace space for Region 3 is obtained as

$$\bar{p}_{D3} = \frac{\bar{p}_{Ds}}{\cosh[\sqrt{s}(x_{D2} - 1)]} \cosh(\sqrt{s}\theta_D). \quad \dots \quad (\text{A-8})$$

The Laplace-transformed differential equation and boundary conditions for the stimulated region are presented as

$$\frac{\partial^2 \bar{p}_{Ds}}{\partial y_D^2} - \frac{R_k}{2} \left(\frac{\partial \bar{p}_{D2}}{\partial x_D} \right)_{x_D=x_{D1}-1} - \frac{R_k}{2} \left(\frac{\partial \bar{p}_{D3}}{\partial \theta_D} \right)_{\theta_D=x_{D2}-1} - sR_\eta \bar{p}_{Ds} = 0, \quad \dots \quad (\text{A-9})$$

$$\bar{p}_{Ds} = \frac{1}{s}, \quad y_D = 0, \quad \dots \quad (\text{A-10})$$

$$\bar{p}_{Ds} = \bar{p}_{D1}(y_{D1}) = \bar{p}_{D1s}, \quad y_D = y_{Ds}, \quad \dots \quad (\text{A-11})$$

where

$$R_k = \frac{k}{k_s}, \quad \dots \quad (\text{A-12})$$

$$R_\eta = \frac{\eta}{\eta_s}. \quad \dots \quad (\text{A-13})$$

By use of Eqs. A-4 and A-8, one may obtain

$$\left(\frac{\partial \bar{p}_{D2}}{\partial x_D} \right)_{x_D=x_{D1}-1} = \bar{p}_{Ds} \sqrt{s} \tanh[\sqrt{s}(x_{D1} - 1)], \quad \dots \quad (\text{A-14})$$

$$\left(\frac{\partial \bar{p}_{D3}}{\partial \theta_D} \right)_{\theta_D=x_{D2}-1} = \bar{p}_{Ds} \sqrt{s} \tanh[\sqrt{s}(x_{D2} - 1)]. \quad \dots \quad (\text{A-15})$$

Replacing Eqs. A-14 and A-15 in Eq. A-9 results in

$$\frac{\partial^2 \bar{p}_{Ds}}{\partial y_D^2} - a_1 \bar{p}_{Ds} = 0, \quad \dots \quad (\text{A-16})$$

where

$$a_1 = \frac{R_k \sqrt{s}}{2} \left\{ \tanh \left[\sqrt{s}(x_{D1} - 1) \right] + \tanh \left[\sqrt{s}(x_{D2} - 1) \right] \right\} + R_\eta s. \quad \dots \quad (\text{A-17})$$

The dimensionless pressure for the stimulated region is therefore obtained as

$$\bar{p}_{Ds} = \frac{1}{s} \cosh(\sqrt{a_1}y_D) + \frac{\bar{p}_{D1s} - \frac{1}{s} \cosh(\sqrt{a_1}y_{Ds})}{\sinh(\sqrt{a_1}y_{Ds})} \sinh(\sqrt{a_1}y_D). \quad \dots \quad (\text{A-18})$$

To obtain dimensionless production rate, we use Darcy's law. From Darcy's law, one can write

$$\bar{q}_{Dw} = -\frac{2}{R_k} \left(\frac{\partial \bar{p}_{Ds}}{\partial y_D} \right)_{y_D=0} \quad (\text{A-19})$$

Therefore,

$$\bar{q}_{Dw} = \frac{2\sqrt{a_1}(a_3 - \bar{p}_{D1s})}{R_k s a_2}, \quad (\text{A-20})$$

where

$$a_2 = \frac{\sinh(\sqrt{a_1} y_{Ds})}{s}, \quad (\text{A-21})$$

$$a_3 = \frac{\cosh(\sqrt{a_1} y_{Ds})}{s}. \quad (\text{A-22})$$

Appendix B—Derivation of Solution for Production Rate: Finite-Conductivity-Fracture Case

Here, the solution for production rate is obtained for a constant-pressure well intersected by a finite-conductivity fracture in a rectangular composite system. Similar to the infinite-conductivity-fracture case, the fracture is placed on the symmetrical line of the system.

For the stimulated region, the transformed differential equation and outer-boundary condition are the same as those for the infinite-conductivity case (Eqs. A-11 and A-16). However, the inner-boundary condition is different. The inner-boundary condition in Laplace space is

$$\bar{p}_{Ds} = \bar{p}_{Df}, \quad y_D = 0. \quad (\text{B-1})$$

Considering Eq. B-1 as the inner-boundary condition, the solution for the stimulated region is obtained as

$$\begin{aligned} \bar{p}_{Ds} = \bar{p}_{Df} \cosh(\sqrt{a_1} y_D) + \frac{\bar{p}_{D1s} - \bar{p}_{Df} \cosh(\sqrt{a_1} y_{Ds})}{\sinh(\sqrt{a_1} y_{Ds})} \\ \times \sinh(\sqrt{a_1} y_D). \end{aligned} \quad (\text{B-2})$$

The differential equation and boundary conditions for the fracture region in Laplace space are

$$\frac{\partial^2 \bar{p}_{Df}}{\partial x_D^2} + \frac{2}{F_{CDs}} \left(\frac{\partial \bar{p}_{Ds}}{\partial y_D} \right)_{y_D=0} - s R_{\eta f} \bar{p}_{Df} = 0, \quad (\text{B-3})$$

$$\frac{\partial \bar{p}_{Df}}{\partial x_D} = 0, \quad x_D = 0, \quad (\text{B-4})$$

$$\bar{p}_{Df} = \frac{1}{s}, \quad x_D = 1, \quad (\text{B-5})$$

where

$$F_{CDs} = \frac{w k_f}{k_s x_f}, \quad (\text{B-6})$$

$$R_{\eta f} = \frac{\eta}{\eta_f}. \quad (\text{B-7})$$

From Eq. B-2, one may obtain

$$\left(\frac{\partial \bar{p}_{Ds}}{\partial y_D} \right)_{y_D=0} = \frac{\sqrt{a_1} [\bar{p}_{D1s} - \bar{p}_{Df} \cosh(\sqrt{a_1} y_{Ds})]}{\sinh(\sqrt{a_1} y_{Ds})}. \quad (\text{B-8})$$

Inserting Eq. B-8 into Eq. B-3 yields

$$\begin{aligned} \frac{\partial^2 \bar{p}_{Df}}{\partial x_D^2} - \left[\frac{2\sqrt{a_1} \cosh(\sqrt{a_1} y_{Ds})}{F_{CDs} \sinh(\sqrt{a_1} y_{Ds})} + s R_{\eta f} \right] \bar{p}_{Df} \\ = -\frac{2\sqrt{a_1}}{F_{CDs} \sinh(\sqrt{a_1} y_{Ds})} \bar{p}_{D1s}, \end{aligned} \quad (\text{B-9})$$

or

$$\frac{\partial^2 \bar{p}_{Df}}{\partial x_D^2} - a_5 \bar{p}_{Df} = -a_6 \bar{p}_{D1s}, \quad (\text{B-10})$$

where

$$a_4 = \coth(\sqrt{a_1} y_{Ds}), \quad (\text{B-11})$$

$$a_5 = \frac{2a_4 \sqrt{a_1}}{F_{CDs}} + s R_{\eta f}, \quad (\text{B-12})$$

$$a_6 = \frac{2\sqrt{a_1}}{F_{CDs} s a_2}. \quad (\text{B-13})$$

Writing the general solution for Eq. B-10 and applying Eqs. B-4 and B-5 to find its constants, the solution for the fracture region is derived as

$$\bar{p}_{Df} = \frac{1}{s} - \frac{a_6}{a_5} \bar{p}_{D1} \cosh(\sqrt{a_5} x_D) + \frac{a_6}{a_5} \bar{p}_{D1s}. \quad (\text{B-14})$$

From Darcy's law, the rate produced from both sides of the system into one-half of the fracture is written as

$$q_w = -\frac{k_f h w}{\mu B} \left(\frac{\partial p_f}{\partial x} \right)_{x=x_f} \quad (\text{B-15})$$

In dimensionless form, Eq. B-15 is expressed as

$$\bar{q}_{Dw} = \frac{F_{CD}}{2} \left(\frac{\partial \bar{p}_{Df}}{\partial x_D} \right)_{x_D=1}, \quad (\text{B-16})$$

where

$$F_{CD} = \frac{w k_f}{x_f k}. \quad (\text{B-17})$$

By use of Eq. B-14 in Eq. B-16, one can write

$$\bar{q}_{Dw} = \frac{1}{2} F_{CD} \sqrt{a_5} \left(\frac{1}{s} - \frac{a_6}{a_5} \bar{p}_{D1s} \right) \tanh(\sqrt{a_5}), \quad (\text{B-18})$$

or

$$\bar{q}_{Dw} = \frac{F_{CD} a_7}{2} (a_5 - s a_6 \bar{p}_{D1s}), \quad (\text{B-19})$$

where

$$a_7 = \frac{\tanh(\sqrt{a_5})}{s \sqrt{a_5}}. \quad (\text{B-20})$$

We must consider the effect of convergence of flow in the fracture toward the well. The additional pressure drop caused by such convergence is (Mukherjee and Economides 1991)

$$\Delta p_{CS} = \frac{q \mu B}{2\pi} \left[\frac{\ln(h/2r_w)}{k_f w} - \frac{\pi}{2k_f w} \right]. \quad (\text{B-21})$$

Therefore, dimensionless pressure drop caused by this skin is

$$p_{D,CS} = \frac{kh}{\pi k_f w} \left[\ln(h/2r_w) - \frac{\pi}{2} \right] = \frac{S_c}{\pi}. \quad (\text{B-22})$$

Note that dimensionless pressure in Eq. B-22 is defined as the reciprocal of dimensionless rate (presented in Table 1). One can write the following trivial equation:

$$(\bar{p}_{Dcr})_C = (\bar{p}_{Dcr})_L + \bar{p}_{D,CS}, \quad (\text{B-23})$$

where C denotes presence of convergence and L denotes the existence of complete linear flow in fracture (no convergence). The relation between dimensionless rate at constant pressure and

dimensionless pressure at constant rate in Laplace space has been reported by van Everdingen and Hurst (1949). We use this relation both for cases where convergence exists and cases where it does not exist. We can write

$$(\bar{q}_{Dcp})_C = \frac{1}{s^2(\bar{p}_{Dcr})_C}, \quad \dots \dots \dots (B-24)$$

$$(\bar{p}_{Dcr})_L = \frac{1}{s^2(\bar{q}_{Dcp})_L}. \quad \dots \dots \dots (B-25)$$

Inserting Eq. B-25 into Eq. B-23 and inserting the obtained equation into Eq. B-24 results in

$$(\bar{q}_{Dcp})_C = \frac{1}{s^2 \left[\frac{1}{s^2(\bar{q}_{Dcp})_L} + \bar{p}_{D,CS} \right]}. \quad \dots \dots \dots (B-26)$$

Replacing the dimensionless rate for the no-convergence condition from Eq. B-19 into Eq. B-26 yields

$$\bar{q}_{Dw} = \frac{1}{s^2 \left\{ \frac{2}{s^2[F_{CD}a_7(a_5 - sa_6\bar{p}_{D1s})]} + \frac{S_c}{\pi s} \right\}}. \quad \dots \dots \dots (B-27)$$

Note that Eq. B-27 represents the produced rate from both sides of the system into one-half of the fracture. Accordingly, Eq. B-27 should be multiplied by two to obtain the rate for total system or representative element, as shown in Fig. 1. The rate is finally obtained as

$$\bar{q}_{Dw} = \frac{1}{\frac{1}{F_{CD}a_7(a_5 - sa_6\bar{p}_{D1s})} + \frac{sS_c}{2\pi}}. \quad \dots \dots \dots (B-28)$$

Appendix C—Derivation of Solution for Pressure Drop Per Unit Rate at the Interface of the Stimulated and Unstimulated Regions

Here, the solution for pressure drop per continuous unit rate at the interface of stimulated and unstimulated regions is derived. The physical system here is Region 1, as seen in Fig. 3. Also, the dimensions and coordinates of the system can be seen in Figs. 2 and 3, respectively. Dimensionless variables are presented in Table 1. The partial-differential equations and boundary conditions in Laplace space for the considered system become

$$\frac{\partial^2 \bar{p}_{D1}}{\partial x_D^2} + \frac{\partial^2 \bar{p}_{D1}}{\partial y_D^2} - s\bar{p}_{D1} = 0, \quad \dots \dots \dots (C-1)$$

$$\frac{\partial \bar{p}_{D1}}{\partial x_D} = 0, \quad x_D = 0, \quad 0 < y_D < y_{D1}, \quad \dots \dots \dots (C-2)$$

$$\frac{\partial \bar{p}_{D1}}{\partial x_D} = 0, \quad x_D = x_{De}, \quad 0 < y_D < y_{D1}, \quad \dots \dots \dots (C-3)$$

$$\frac{\partial \bar{p}_{D1}}{\partial y_D} = 0, \quad 0 < x_D < x_{De}, \quad y_D = 0, \quad \dots \dots \dots (C-4)$$

$$\frac{\partial \bar{p}_{D1}}{\partial y_D} = \begin{cases} 0, & 0 < x_D < x_{D1} - 1, \quad x_{D1} + 1 < x_D < x_{De} \\ \frac{1}{s}, & x_{D1} - 1 < x_D < x_{D1} + 1 \end{cases}, \quad y_D = y_{D1}. \quad \dots \dots \dots (C-5)$$

To eliminate differentiation with respect to the x -coordinate, we use the finite Fourier cosine transform. This transformation was used by Odeh (1968) for obtaining a production solution from wells with limited entry to flow. Here, we use this transformation for our specific problem. Finite Fourier cosine transform is defined as

$$\mathcal{F}_c \left[f(z) \right] = \tilde{f}(n) = \int_0^l f(z) \cos \left(\frac{n\pi}{l} z \right) dz. \quad \dots \dots \dots (C-6)$$

The inversion formula is

$$f(z) = \frac{1}{l} \left[\tilde{f}(0) + 2 \sum_{n=1}^{\infty} \tilde{f}(n) \cos \left(\frac{n\pi}{l} z \right) \right]. \quad \dots \dots \dots (C-7)$$

The dimensionless pressure in Laplace and Fourier space is defined as

$$\tilde{\bar{p}}_{D1}(n, y_D, s) = \int_0^{x_{De}} \bar{p}_{D1}(x_D, y_D, s) \cos \left(\frac{n\pi}{x_{De}} x_D \right) dx_D. \quad \dots \dots (C-8)$$

From the definition of Fourier cosine transform, one can write

$$\mathcal{F}_c \left\{ \frac{\partial^2 \bar{p}_{D1}}{\partial x_D^2} \right\} = (-1)^n \left(\frac{\partial \bar{p}_{D1}}{\partial x_D} \right)_{x_D=x_{De}} - \left(\frac{\partial \bar{p}_{D1}}{\partial x_D} \right)_{x_D=0} - \left(\frac{n\pi}{x_{De}} \right)^2 \tilde{\bar{p}}_{D1}. \quad \dots \dots \dots (C-9)$$

Considering Eqs. C-2 and C-3, Eq. C-9 becomes

$$\mathcal{F}_c \left(\frac{\partial^2 \bar{p}_{D1}}{\partial x_D^2} \right) = - \left(\frac{n\pi}{x_{De}} \right)^2 \tilde{\bar{p}}_{D1}, \quad \dots \dots \dots (C-10)$$

Taking the Fourier transform from Eq. C-1 results in

$$\frac{\partial^2 \tilde{\bar{p}}_{D1}}{\partial y_D^2} - \left(\frac{n\pi}{x_{De}} \right)^2 \tilde{\bar{p}}_{D1} - s\tilde{\bar{p}}_{D1} = 0, \quad \dots \dots \dots (C-11)$$

or

$$\frac{\partial^2 \tilde{\bar{p}}_{D1}}{\partial y_D^2} - \xi_n^2 \tilde{\bar{p}}_{D1} = 0, \quad \dots \dots \dots (C-12)$$

where

$$\xi_n^2 = \left(\frac{n\pi}{x_{De}} \right)^2 + s. \quad \dots \dots \dots (C-13)$$

Eq. C-4 in the Laplace and Fourier domains becomes

$$\frac{\partial \tilde{\bar{p}}_{D1}}{\partial y_D} = 0, \quad 0 < x_D < x_{De}, \quad y_D = 0. \quad \dots \dots \dots (C-14)$$

At $y_D = y_{D1}$, we can write

$$\begin{aligned} \left(\frac{\partial \tilde{\bar{p}}_{D1}}{\partial y_D} \right)_{y_D=y_{D1}} &= \int_0^{x_{De}} \frac{\partial \bar{p}_{D1}}{\partial y_D} \cos \left(\frac{n\pi}{x_{De}} x_D \right) dx_D \\ &= \int_0^{x_{D1}-1} \frac{\partial \bar{p}_{D1}}{\partial y_D} \cos \left(\frac{n\pi}{x_{De}} x_D \right) dx_D + \int_{x_{D1}-1}^{x_{D1}+1} \frac{\partial \bar{p}_{D1}}{\partial y_D} \cos \left(\frac{n\pi}{x_{De}} x_D \right) dx_D \\ &\quad + \int_{x_{D1}+1}^{x_{De}} \frac{\partial \bar{p}_{D1}}{\partial y_D} \cos \left(\frac{n\pi}{x_{De}} x_D \right) dx_D. \quad \dots \dots \dots (C-15) \end{aligned}$$

In Eq. C-15, the first and third integrals are zero, and Eq. C-5 is inserted into the second integral. Therefore, Eq. C-15 in the Laplace and Fourier domains is expressed as

$$\left(\frac{\partial \tilde{\bar{p}}_{D1}}{\partial y_D} \right)_{y_D=y_{D1}} = \frac{x_{De}}{n\pi s} \left\{ \sin \left[\frac{n\pi}{x_{De}} (x_{D1} + 1) \right] - \sin \left[\frac{n\pi}{x_{De}} (x_{D1} - 1) \right] \right\}. \quad \dots \dots \dots (C-16)$$

The general solution for Eq. C-12 is

$$\tilde{p}_{D1} = A \sinh(\xi_n y_D) + B \cosh(\xi_n y_D). \quad (C-17)$$

By use of Eqs. C-14 and C-16, one can obtain the constants in Eq. C-17. Obtaining the unknowns and replacing them in Eq. C-17, the solution in the Laplace and Fourier domains is obtained as

$$\tilde{p}_{D1}(n, y_D, s) = \frac{x_{De} \left\{ \sin \left[\frac{n\pi}{x_{De}} (x_{D1} + 1) \right] - \sin \left[\frac{n\pi}{x_{De}} (x_{D1} - 1) \right] \right\}}{n\pi s \xi_n \sinh(\xi_n y_{D1})} \times \cosh(\xi_n y_D). \quad (C-18)$$

From the Fourier inversion formula (Eq. C-7), the solution in Laplace domain is

$$\bar{p}_{D1}(x_D, y_D, s) = \frac{1}{x_{De}} \left[\tilde{p}_{D1}(0, y_D, s) + 2 \sum_{n=1}^{\infty} \tilde{p}_{D1}(n, y_D, s) \cos \left(\frac{n\pi}{x_{De}} x_D \right) \right]. \quad (C-19)$$

Knowing that,

$$\lim_{n \rightarrow 0} \frac{\sin n}{n} = 1. \quad (C-20)$$

Thus,

$$\tilde{p}_{D1}(0, y_D, s) = \frac{2 \cosh(\sqrt{s} y_D)}{s \sqrt{s} \sinh(\sqrt{s} y_{D1})}. \quad (C-21)$$

Inserting Eqs. C-18 and C-21 into Eq. C-19 results in

$$\begin{aligned} \bar{p}_{D1}(x_D, y_D, s) &= \frac{1}{x_{De}} \left(\frac{2 \cosh(\sqrt{s} y_D)}{s \sqrt{s} \sinh(\sqrt{s} y_{D1})} \right. \\ &+ \frac{2 x_{De}}{\pi s} \sum_{n=1}^{\infty} \left\{ \frac{\sin \left[\frac{n\pi}{x_{De}} (x_{D1} + 1) \right] - \sin \left[\frac{n\pi}{x_{De}} (x_{D1} - 1) \right]}{n \xi_n \sinh(\xi_n y_{D1})} \right\} \\ &\times \cosh(\xi_n y_D) \cos \left(\frac{n\pi}{x_{De}} x_D \right) \Big). \quad (C-22) \end{aligned}$$

The pressure at distance y_{D1} would be

$$\begin{aligned} \bar{p}_{D1}(x_D, y_{D1}, s) &= \frac{2 \coth(\sqrt{s} y_{D1})}{x_{De} s \sqrt{s}} \\ &+ \frac{2}{\pi s} \sum_{n=1}^{\infty} \left\{ \frac{\sin \left[\frac{n\pi}{x_{De}} (x_{D1} + 1) \right] - \sin \left[\frac{n\pi}{x_{De}} (x_{D1} - 1) \right]}{n \xi_n} \right\} \\ &\times \coth(\xi_n y_{D1}) \cos \left(\frac{n\pi}{x_{De}} x_D \right). \quad (C-23) \end{aligned}$$

We use the following equation to obtain average pressure with respect to x_D distance open to flow:

$$\bar{p}_{D1}(y_{D1}, s) = \frac{1}{2} \int_{x_{D1}-1}^{x_{D1}+1} \bar{p}_D dx_D. \quad (C-24)$$

The final solution is

$$\begin{aligned} \bar{p}_{D1,u}(y_{D1}) &= \bar{p}_{D1,s,u} = \frac{2 \coth(\sqrt{s} y_{D1})}{x_{De} s \sqrt{s}} \\ &+ \frac{2 x_{De}}{\pi^2 s} \sum_{n=1}^{\infty} \left\{ \frac{\sin \left[\frac{n\pi}{x_{De}} (x_{D1} + 1) \right] - \sin \left[\frac{n\pi}{x_{De}} (x_{D1} - 1) \right]}{n^2 \xi_n} \right\}^2 \\ &\times \coth(\xi_n y_{D1}). \quad (C-25) \end{aligned}$$

Appendix D—Derivation of Actual Pressure Drop at the Interface of Stimulated and Unstimulated Regions

In Appendix C, the pressure drop at the interface of stimulated and unstimulated regions was derived for removal of a unit flux per unit area. For the condition of constant well pressure, the rate exiting Region 1 is not constant. Therefore, we use the convolution integral to obtain pressure drop at the exit of Region 1 for this variable rate. We can write

$$\Delta p_{1s} = \int_0^t q_1(\tau) \frac{\partial \Delta p_{1s,u}(t-\tau)}{\partial \tau} d\tau, \quad (D-1)$$

where q_1 is the flow rate exiting unstimulated region and entering stimulated region and may be expressed as

$$q_1 = \frac{2k_s h x_f}{\mu B} \left(\frac{\partial p_s}{\partial y} \right)_{y=y_s} \quad (D-2)$$

Writing Eq. D-1 in dimensionless form would be

$$p_{D1s}(t_D) = -\frac{1}{R_k} \int_0^{t_D} \frac{\partial p_{D1s,u}(t_D - \tau)}{\partial \tau} \left(\frac{\partial p_{Ds}}{\partial y_D} \right)_{y_D=y_{Ds}} d\tau. \quad (D-3)$$

Taking Laplace from Eq. D-3, one may obtain

$$\bar{p}_{D1s} = -\frac{1}{R_k} s \bar{p}_{D1s,u} \left(\frac{\partial \bar{p}_{Ds}}{\partial y_D} \right)_{y_D=y_{Ds}} \quad (D-4)$$

For the infinite-conductivity-fracture case, we use Eq. A-18. Therefore, we may write

$$\left(\frac{\partial \bar{p}_{Ds}}{\partial y_D} \right)_{y_D=y_{Ds}} = \sqrt{a_1} [a_2 + (\bar{p}_{D1s} - a_3) a_4]. \quad (D-5)$$

Inserting Eq. D-5 into Eq. D-4 yields

$$\bar{p}_{D1s} = -\frac{s \sqrt{a_1} \bar{p}_{D1s,u}}{R_k} [a_2 + (\bar{p}_{D1s} - a_3) a_4]. \quad (D-6)$$

Therefore, the dimensionless pressure at the interface is obtained as

$$\bar{p}_{D1s} = \frac{a_3 a_4 - a_2}{\frac{R_k}{s \sqrt{a_1} \bar{p}_{D1s,u}} + a_4}. \quad (D-7)$$

To find the pressure drop at the interface for the finite-conductivity-fracture case, we should use Eq. B-2. From this equation, one may write

$$\left(\frac{\partial \bar{p}_{Ds}}{\partial y_D} \right)_{y_D=y_{Ds}} = \sqrt{a_1} \left[\bar{p}_{Df} s a_2 + (\bar{p}_{D1s} - \bar{p}_{Df} s a_3) a_4 \right]. \quad (D-8)$$

Inserting Eq. D-8 into Eq. D-4 results in

$$\bar{p}_{D1s} = -\frac{s \sqrt{a_1}}{R_k} \bar{p}_{D1s,u} \left[\bar{p}_{Df} s a_2 + (\bar{p}_{D1s} - \bar{p}_{Df} s a_3) a_4 \right]. \quad (D-9)$$

We should set an average value for dimensionless pressure drop in the fracture:

$$\bar{p}_{Df,ave} = \int_0^1 \bar{p}_{Df} dx_D. \quad (D-10)$$

Applying Eq. D-10 on Eq. B-14, we obtain

$$\bar{p}_{Df,ave} = \left(\frac{1}{s\sqrt{a_5}} - \frac{a_6}{a_5\sqrt{a_5}} \bar{p}_{D1s} \right) \tanh(\sqrt{a_5}) + \frac{a_6}{a_5} \bar{p}_{D1s}, \quad \dots \dots \dots (D-11)$$

or

$$\bar{p}_{Df,ave} = a_7 + \frac{a_6}{a_5} (1 - sa_7) \bar{p}_{D1s}, \quad \dots \dots \dots (D-12)$$

where

$$a_7 = \frac{\tanh(\sqrt{a_5})}{s\sqrt{a_5}}. \quad \dots \dots \dots (D-13)$$

Inserting dimensionless average fracture pressure into Eq. D-9 results in

$$\begin{aligned} \bar{p}_{D1s} = & -\frac{s\sqrt{a_1}}{R_k} \bar{p}_{D1s,u} \left\{ \left[a_7 + \frac{a_6}{a_5} (1 - sa_7) \bar{p}_{D1s} \right] sa_2 + \bar{p}_{D1s} a_4 \right. \\ & \left. - \left[a_7 + \frac{a_6}{a_5} (1 - sa_7) \bar{p}_{D1s} \right] sa_3 a_4 \right\}. \quad \dots \dots \dots (D-14) \end{aligned}$$

Finally, the dimensionless pressure drop at the interface for a finite-conductivity-fracture case is obtained as

$$\begin{aligned} \bar{p}_{D1s} = & \frac{sa_7(a_3a_4 - a_2)}{\frac{R_k}{s\sqrt{a_1}\bar{p}_{D1s,u}} + a_4 + \frac{a_6a_2}{a_5}s - \frac{a_6a_2a_7}{a_5}s^2 - \frac{a_6a_3a_4}{a_5}s + \frac{a_6a_7a_3a_4}{a_5}s^2}. \quad \dots \dots \dots (D-15) \end{aligned}$$

Appendix E—Comparison of Presented Enhanced-Fracture-Region (EFR) Model With Previous Ones and Discussion About Its Accuracy

Compared with our new model, the trilinear-flow (TLF) model (Brown et al. 2011) has two major limitations. First, it is only capable of modeling cases in which the stimulated region covers the entire interface region. In another words, considering the definitions in Fig. 2, it can only handle problems where $y_s = y_e$. Second, the TLF model assumes that there are equally spaced laterals ($x_l = x_2 = x_e/2$ in Fig. 2), which is not actually always valid when

Case No.	$x_{D1} (x_{De}/2)$	y_{De}	y_{Ds}
1	2	2	0.2
2	4	4	0.2
3	8	8	0.2
4	2	2	1
5	4	4	1
6	8	8	1
7	4	4	3
8	8	4	1

Table E-1—Data for Cases 1 through 8. For all cases, $x_f = 50$ ft, $k = 0.001$, and $k_s = 0.005$. The other properties can be obtained from Table 3.

dealing with real-world (field) examples. Although the previous EFR model (Stalgorova and Mattar 2013) has solved the first limitation of the TLF model, it still has the second limitation: It is unable to model cases in which the boundaries on either side of the well are not equally spaced. Furthermore, the new EFR model accounts for the radial (2D) nature of flow in Region 1 (Fig. 3), whereas in the previous EFR model this region was divided into two regions with a 1D flow assumption in each region (which are perpendicular to each other). As mentioned in Stalgorova and Mattar (2013), their EFR model is not applicable for the cases where the stimulated region is too small and/or the distance from the well to its parallel boundaries is not large.

We tested our EFR model for a wide range of parameters and observed that it is more accurate than the previous EFR model. We used Eq. 19 to convert the previous EFR model to be applicable for constant-pressure production because it was developed originally for constant-rate production. An example comparison has been provided in Fig. E-1, in which derivative plots for numerical simulation, the new EFR solution (this paper), and the Stalgorova and Mattar (2013) EFR solution for three cases (Cases 1, 2, and 3) are given. The properties of these cases, which only differ in the size of the external boundaries of the physical model, are presented in Table E-1. For all these three cases, $y_{Ds} = 0.2$. As can be observed from Fig. E-1, the new solution is in good agreement with the numerical model results, whereas the previous EFR solution exhibits a discrepancy with the numerical solution. As the size of reservoir increases, this discrepancy increases. We considered a wide range of reservoir dimensions to test accuracy of our solutions and found that they are acceptable in almost all ranges of parameters. However, the solutions become less accurate in certain specific ranges of parameters. Although the new solutions may not show excellent accuracy in that range, they are still more accurate than the previous EFR model for the considered range. An example is presented in Fig. E-2, in which the

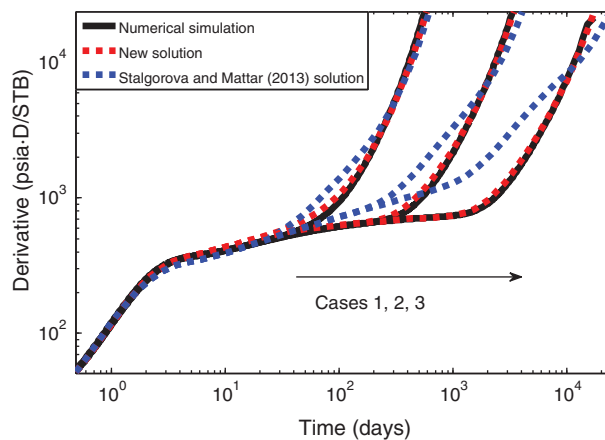


Fig. E-1—Comparison of numerical simulation, new solution, and Stalgorova and Mattar (2013) solution for Cases 1, 2, and 3.

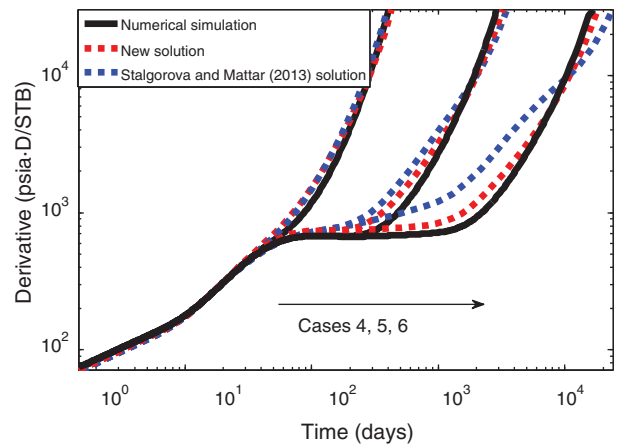


Fig. E-2—Comparison of numerical simulation, new solution, and Stalgorova and Mattar (2013) solution for Cases 4, 5, and 6.

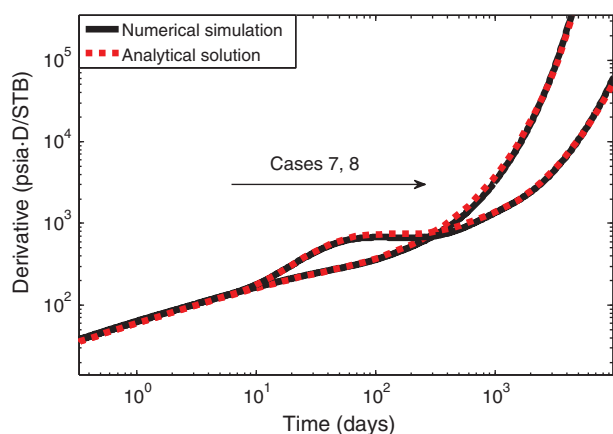


Fig. E-3—Comparison of numerical simulation and new solution for Cases 7 and 8.

new EFR solution and previous EFR solution are compared with the numerical simulation for Cases 4 through 6. It is seen that as the size of the reservoir increases, the accuracy of both the new solution and Stalgorova and Mattar (2013) solution decreases. Cases 4 through 6 in Fig. E-2 have the same properties as Cases 1 through 3 in Fig. E-1, except for the size of the stimulated zone. In Fig. E-1, $y_{Ds} = 0.2$, whereas in Fig. E-2, $y_{Ds} = 1$. Accordingly, for a given reservoir, one may conclude that as the size of stimulated zone increases, the accuracy of solutions decreases. However, it is not completely true because as the size of the stimulated zone exceeds a certain value, the solutions tend to be more accurate. This can be understood from comparison of the accuracy of the solutions for Case 7 in Fig. E-3 and Case 5 in Fig. E-2. The properties of both cases are the same except that the size of stimulated zone in Case 7 is three times greater than that of Case 5. We may expect that increasing the size of the stimulated zone decreases the accuracy of the solution, but here we observe the opposite behavior (i.e., plot of Case 7 exhibits a better accuracy). Also, Case 8 in Fig. E-3 and Case 5 in Fig. E-2 have the same properties except x_{D1} in Case 8 is two times greater than that of Case 5. In another words, in Case 5 $x_{D1} = y_{De}$, whereas in Case 8 $x_{D1} = 2y_{De}$. Considering that Case 8 shows more accuracy than Case 5, one may conclude that even for moderate to high values

of y_{Ds} and y_{De} , if x_{D1} is much greater than y_{De} , the new solution tends to exhibit good accuracy. In summary, the new solutions may not show excellent accuracy when all the following conditions are met: y_{De} is very large, y_{De} is nearly equal to or greater than x_{D1} , and the value of y_{Ds} is in a moderate range (not small and not large compared with y_{De}). If one of the mentioned conditions is violated, accuracy of the solutions increases.

Mohammadhossein Heidari Sureshjani is a reservoir engineer. His research interests are in gas and gas/condensate reservoir engineering, and production-data analysis of oil and gas reservoirs. Sureshjani has published several conference and peer-reviewed-journal articles on the topic of production-data analysis. He is an SPE member. Sureshjani holds a master's degree from Petroleum University of Technology, Iran, and a master's degree from the University of Calgary, both in petroleum reservoir engineering.

Christopher R. Clarkson is a professor and the AITF Shell/Encana Chair in Unconventional Gas and Light Oil research in the Department of Geoscience and an adjunct professor with the Department of Chemical and Petroleum Engineering at the University of Calgary. His professional focus in the industry was the exploration for and development of unconventional gas and light-oil reservoirs. Clarkson's research focus since joining the University of Calgary in 2009 has been on advanced reservoir-characterization methods for unconventional gas and light oil, such as rate- and pressure-transient analysis, flow-back analysis, and core analysis. He is also interested in simulation of enhanced-recovery processes in unconventional gas and light oil, and how these processes can be used to reduce greenhouse-gas emissions. Clarkson leads an industry-sponsored consortium, the Tight Oil Consortium, which is focused on these research topics for unconventional light-oil reservoirs in North America. The author of numerous articles in peer-reviewed scientific and engineering journals, Clarkson received the Rossiter W. Raymond Memorial Award from AIME and the Alfred Noble Prize from the American Society of Civil Engineers for his study, "Application of a New Multicomponent Adsorption Model to Coal Gas Adsorption Systems," which was published in *SPE Journal* in September 2003. He was an SPE Distinguished Lecturer for the 2009–2010 season and is currently serving as an associate editor for *Journal of Canadian Petroleum Technology*. Clarkson holds a PhD degree in geological engineering from the University of British Columbia, Canada.